2007

Variations in 24-mu m morphologies among galaxies in the Spitzer Infrared Nearby Galaxies Survey: new insights into the Hubble sequence

GJ Bendo

D Calzetti

CW Engelbracht

RC Kennicutt

MJ Meyer

See next page for additional authors

Recommended Citation

Bendo, GJ; Calzetti, D; Engelbracht, CW; Kennicutt, RC; Meyer, MJ; Thornley, MD; Walter, F; Dale, DA; Li, A; and Murphy, EJ, "Variations in 24-mu m morphologies among galaxies in the Spitzer Infrared Nearby Galaxies Survey: new insights into the Hubble sequence" (2007). *MONTHLY NOTICES OF THE ROYAL ASTRONOMICAL SOCIETY*. 150.
https://doi.org/10.1111/j.1365-2966.2007.12204.x

Mon. Not. R. Astron. Soc. **000**, 1–26 () Printed 1 February 2008 (MN LATEX style file v2.2)

Variations in 24 μm morphologies among galaxies in the *Spitzer* Infrared Nearby Galaxies Survey: New insights into the Hubble sequence

G. J. Bendo,[1], D. Calzetti,[2], C. W. Engelbracht,[3] R. C. Kennicutt, Jr.,[4], M. J. Meyer,[5] M. D. Thornley,[6] F. Walter,[7] D. A. Dale,[8] A. Li,[9] and E. J. Murphy[10]
[1] *Astrophysics Group, Imperial College, Blackett Laboratory, Prince Consort Road, London SW7 2AZ, United Kingdom*
[2] *Department of Astronomy, University of Massachusetts, LGRT-B 254, 710 North Pleasant Street, Amherst, MA 01002, USA*
[3] *Steward Observatory, University of Arizona, 933 North Cherry Avenue, Tucson, AZ 85721, USA*
[4] *Institute of Astronomy, University of Cambridge, Cambridge CB3 0HA, United Kingdom*
[5] *Space Telescope Science Institute, 3700 San Martin Drive, Baltimore, MD 21218, USA*
[6] *Department of Physics & Astronomy, Bucknell University, Lewisburg, PA 17837, USA*
[7] *Max-Planck-Institut für Astronomie, Königstuhl 17, D-69117 Heidelberg, Germany*
[8] *Department of Physics and Astronomy, University of Wyoming, Laramie, WY 82071, USA*
[9] *Department of Physics and Astronomy, University of Missouri, Columbia, MO 65211, USA*
[10] *Department of Astronomy, Yale University, P.O. Box 208101, New Haven, CT 06520, USA*

ABSTRACT
To study the distribution of star formation and dust emission within nearby galaxies, we measured five morphological parameters in the 3.6 and 24 μm wave bands for 65 galaxies in the *Spitzer* Infrared Nearby Galaxies Survey (SINGS) and 8 galaxies that were serendipitously observed by SINGS. The morphological parameters demonstrate strong variations along the Hubble sequence, including statistically significant differences between S0/a-Sab and Sc-Sd galaxies. Early-type galaxies are generally found to be compact, centralized, symmetric sources in the 24 μm band, while late-type galaxies are generally found to be extended, asymmetric sources. These results suggest that the processes that increase the real or apparent sizes of galaxies' bulges also lead to more centralized 24 μm dust emission. Several phenomena, such as strong nuclear star formation, Seyfert activity, or outer ring structures, may cause galaxies to deviate from the general morphological trends observed at 24 μm. We also note that the 24 μm morphologies of Sdm-Im galaxies are quite varied, with some objects appearing very compact and symmetric while others appear diffuse and asymmetric. These variations reflect the wide variation in star formation in irregular galaxies as observed at other wavelengths. The variations in the 24 μm morphological parameters across the Hubble sequence mirror many of the morphological trends seen in other tracers of the ISM and in stellar emission. However, the 24 μm morphological parameters for the galaxies in this sample do not match the morphological parameters measured in the stellar wave bands. This implies that the distribution of dust emission is related to but not equivalent to the distribution of stellar emission.

Key words: infrared:galaxies, galaxies:ISM, galaxies: structure

1 INTRODUCTION

The variations in the integrated properties of the interstellar medium (ISM) and integrated star formation activity along the Hubble sequence is clearly defined. Roberts & Haynes (1994) and references therein have shown that the total gas surface density and the ratio of gas mass to total mass increases when proceeding along the Hubble sequence from elliptical galaxies through early-type spiral galaxies (galaxies with large bulges and tightly-wound arms) to late-type spiral galaxies (galaxies with small or negligible bulges and loosely-wound arms). Kennicutt (1998a) and references therein have used various tracers of star formation normalized by total stellar content to establish the general increase in star formation activity when proceeding from elliptical galaxies to late-type spiral galaxies along the Hubble sequence. Moreover, all of these trends show significant differences in the in-

terstellar content and star formation activity between early- and late-type spiral galaxies.

However, few investigations have carefully studied whether the spatial distribution of the ISM or star formation varies among spiral galaxies, particularly between Sa and Sd galaxies. Hodge & Kennicutt (1983) show that the radial distributions of HII regions are broader in late-type than in early-type spiral galaxies, but their sample only contains 37 galaxies and includes no galaxies earlier than Sb. Later Hα surveys appear to contradict these results; a larger Hα survey by (Dale et al. 2001a) found no variations in the radial extent of the Hα emission normalized by the spatial extent of the I-band emission, and another Hα survey by Koopmann et al. (2006) found no variations in the ratio of the Hα/R-band scale lengths. Bendo et al. (2002) and Thomas et al. (2004) did demonstrate that the dust emission was more extended in late-type spiral galaxies than in early-type spiral galaxies, but the data in Bendo et al. (2002) did not include all of the galaxy emission, and the sample in Thomas et al. (2004) contained very few galaxies with Hubble types earlier than Sb. Pahre et al. (2004) qualitatively show a similar variation in the non-stellar 8.0 μm morphology of galaxies across the Hubble sequence but did not apply a quantitative analysis. Young et al. (1995) did demonstrate strong variations in the CO emission across the Hubble sequence, but the observations consisted mostly of a series of single low-resolution pointed observations along the major axes of the target galaxies. In contrast to these other observations, Thomas et al. (2004) observed that the spatial extent of HI emission did not vary with Hubble type, at least between Sb and Sd galaxies.

Variations in the distribution of the ISM and star formation among spiral galaxies could have fundamental implications for the stellar evolution and the evolution of structure within galaxies. Moreover, such variations may provide clues to the processes that form galaxies' disks and bulges. For example, if the ISM is more centrally concentrated in early-type spiral galaxies than in late-type spiral galaxies, this may point to merger phenomena as having formed the bulges of early-type spiral galaxies and causing gas to fall into the galaxies' nuclei (e.g. Schweizer 1998), or it may indicate that the centres of early-type galaxies contain pseudobulges, which form through secular processes that funnel gas into the nuclei and trigger nuclear star formation activity (e.g. Kormendy & Kennicutt 2004). Also note that the distribution of dust emission may be related to other galaxy properties. For example, Dale et al. (2007) demonstrated that the clumpiness and central concentration of 24 μm emission was linked to the dust temperatures and the ratio of infrared to ultraviolet luminosity. Links between the distribution of dust and galaxy morphology may therefore have implications for how other galaxy properties vary along the Hubble sequence as well.

The *Spitzer* Infrared Nearby Galaxies Survey (SINGS; Kennicutt et al. 2003) recently completed mid- and far-infrared observations of nearby galaxies that represent a cross section of galaxies with different Hubble types, luminosities, and infrared/optical ratios. Additionally, this survey detected many serendipitous sources, including nearby galaxies not included in the SINGS sample. In this paper, we use the 24 μm *Spitzer* data to understand how the distribution of this component of dust emission varies among nearby galaxies. For comparison with stellar morphologies, we also examine the morphologies in the 3.6 μm images, which trace stellar emission that mostly originates from evolved stellar populations (e.g. Lu et al. 2003).

In general, infrared dust emission can be used as an approximate tracer of both star formation and interstellar dust mass. Technically, dust emission represents the fraction of the total stellar radiation that is absorbed by dust. However, since hot young stars frequently produce a significant fraction of the total bolometric luminosity within star formation regions and since dust is concentrated near star formation regions, dust emission is an effective star formation tracer. This has been demonstrated recently with comparisons between *Spitzer Space Telescope* 8 - 160 μm data and Hα or ultraviolet emission in nearby galaxies including M 81 (Gordon et al. 2004; Perez-Gonzalez et al. 2006) and M 51 (Calzetti et al. 2005). The 24 μm wave band, which originated from both transiently-heated very small grain and grains that are in thermal equilibrium at $\sim$ 100 K, appears to be the best star formation tracer of all the IRAC and MIPS bands. While the 24 μm band is particularly sensitive to dust heating (Dale et al. 2001b; Li & Draine 2001) and may therefore be less than ideal for tracing dust mass, the high spatial resolution (6 arcsec) and signal-to-noise ratios in the 24 μm data are superior to any other mid- or far-infrared data available from *Spitzer* or elsewhere. The 24 μm data are therefore the best data available at this time for studying the spatial distribution of dust in nearby galaxies. Note that the 24 μm emission may not trace star formation very well in some dwarf galaxies with stochastic star formation (e.g. Cannon et al. 2005, 2006) and active galactic nuclei may be responsible for significant amounts of dust heating in the nuclei of some galaxies (e.g. Bendo et al. 2006, for an extreme example), but the 24 μm emission can still provide some information on star formation even in these cases.

In Section 2, we discuss the sample used for the analysis, the *Spitzer* observations with the Infrared Array Camera (IRAC; Fazio et al. 2004) and the Multiband Imaging Photometer for *Spitzer* (MIPS; Rieke et al. 2004), the data reduction and the parameterization of the morphologies of the target galaxies. We rely on the morphological parameters defined by Conselice (2003) and Lotz et al. (2004) as well as the half-light radius of the 24 μm emission normalized by optical radius to study the morphologies. In Section 3, we examine the effects of distance and inclination angle on these parameters, and we derive corrections for dealing with these effects where necessary. In Section 4, we study how the morphological parameters vary along the Hubble sequence, with particular emphasis placed on searching for variation in morphology from S0/a-Sab through to Sc-Scd spiral galaxies, and we also select galaxies with representative or peculiar 24 μm morphologies for their Hubble types. We briefly compare the 24 μm morphologies of barred and unbarred spiral galaxies in Section 5. We then discuss in Section 6 how the results compare to previous studies of the ISM and optical morphologies and what the implications are for interpreting the Hubble sequence. A summary of the results is presented in Section 7.

2 DATA

2.1 Sample

The sample is selected from the SINGS sample of galaxies as well as additional sources that were serendipitously observed in the SINGS MIPS observations. For a description of the SINGS sample, see Kennicutt et al. (2003).

A few SINGS sources were not suitable for this analysis. We excluded sources with surface brightnesses that did not exceed three times the background noise in any MIPS wave bands. This step not only excludes non-detections but also galaxies where the primary source of 24 μm emission may be starlight. The dwarf irregular galaxies DDO 154, DDO 165, Ho IX, M81 Dwarf A, and M81 Dwarf B as well as the elliptical galaxies NGC 584 and NGC 4552 are thus excluded from the sample. NGC 1404 was excluded because the only significant source of emission within the optical disc at 70 and 160 μm is a point source to the northeast of the nucleus that may not be physically associated with the galaxy. NGC 5195 (M51b) was excluded because a significant fraction of the emission within its optical disc originates from NGC 5194 (M51a). NGC 3034 (M82) was excluded because the source saturated the 24 μm image. The resulting sample contains 65 galaxies.

Although a large number of serendipitous sources were detected in this survey, we placed several constraints on the serendipitous sources that could be used for this study. First, we only used sources listed in the Third Reference Catalogue of Bright Galaxies (RC3; de Vaucouleurs et al. 1991) that are within 2500 km/s (the approximate maximum redshift for the SINGS sample). Next, we required the sources to have surface brightnesses that exceeded three times the background noise in all MIPS wave bands. Finally, we excluded NGC 2799 because the optical disc of the galaxy contains significant emission from the point spread function of the emission from NGC 2798. The final sample of serendipitous sources contains 8 galaxies.

Basic properties of the sample galaxies are listed in Tables 1 and 2. Note that this sample is not an unbiased sample of nearby galaxies. The SINGS sample is not chosen to be a representative cross-section of nearby galaxies but instead is chosen to contain nearby galaxies with a broad range of properties, including a broad range of infrared luminosities and a broad range of optical to infrared luminosity ratios. Some of the galaxies that were included in SINGS to completely sample this colour and luminosity space may be unusual compared to the majority of nearby galaxies. The serendipitous sources tend to be late-type galaxies that are physically associated with the SINGS galaxies, so they also may not necessarily be representative of nearby galaxies in general. As a consequence, any trends versus Hubble type for this sample may be noisier than for an unbiased sample of galaxies such as a distance-limited sample. Nonetheless, since the sample used in this paper still contains many average nearby galaxies, the sample should still be useful for probing the infrared morphologies of nearby galaxies.

2.2 Observations and Data Reduction

The 3.6 and 24 μm data were taken with *Spitzer* as part of the SINGS legacy project. The 3.6 μm IRAC observations for each object consist of either a series of 5 arcmin

Table 1. Basic Properties of the Sample Galaxies from SINGS

Name	Hubble Type[a]	Size of Optical Disc (arcmin)[a]	Distance (Mpc)[b]
DDO 53	Im	1.5×1.3[c]	3.5
Ho I	IAB(s)m	3.6×3.6[d]	3.5
Ho II	Im	7.9×6.3	3.5
IC 2574	SAB(s)m	13.2×5.4	3.5
IC 4710	SB(s)m	3.6×2.8	8.5
Mrk 33	Im pec	1.0×0.9[d]	21.7
NGC 24	SA(s)c	5.8×1.3	8.2
NGC 337	SB(s)d	2.9×1.8	24.7
NGC 628	SA(s)c	10.5×9.5	11.4
NGC 855	E	2.6×1.0	9.6
NGC 925	SAB(s)d	10.5×5.9	10.1
NGC 1097 [e]	SB(s)b	9.3×6.3	16.9
NGC 1266	(R')SB0(rs) pec	1.5×1.0[d]	31.3
NGC 1291	(R)SB(s)0/a	9.8×8.1[d]	9.7
NGC 1316	SAB(s)0 pec	12.0×8.5	26.3
NGC 1377	S0	1.8×0.9	24.4
NGC 1482	$SA0^+$ pec	2.5×1.4	22.0
NGC 1512	SB(r)a	8.9×5.6	10.4
NGC 1566	SAB(s)bc	8.3×6.6	18.0
NGC 1705	$SA0^-$ pec	1.9×1.4	5.8
NGC 2403	SAB(s)cd	21.9×12.3	3.5
NGC 2798	SB(s)a pec	2.6×1.0	24.7
NGC 2841	SA(r)b	8.1×3.5	9.8
NGC 2915	I0	1.9×1.0	2.7
NGC 2976	SAc pec	5.9×2.7	3.5
NGC 3031	SA(s)ab	26.9×14.1	3.5
NGC 3049	SB(rs)ab	2.2×1.4	19.6
NGC 3184	SAB(rs)cd	7.4×6.9	8.6
NGC 3190	SA(s)a pec	4.4×1.5	17.4
NGC 3198	SB(rs)c	8.5×3.3	9.8
NGC 3265	E	1.3×1.0	20.0
NGC 3351	SB(r)b	7.4×5.0	9.3
NGC 3521	SAB(rs)bc	11.0×5.1	9.0
NGC 3621	SA(s)d	12.3×7.1	6.2
NGC 3627	SAB(s)b	9.1×4.2	8.9
NGC 3773	SA0	1.2×1.0	12.9
NGC 3938	SA(s)c	5.4×4.9[d]	12.2
NGC 4125	E6 pec	5.8×3.2	21.4
NGC 4236	SB(s)dm	21.9×7.2	3.5
NGC 4254	SA(s)c	5.4×4.7[d]	20.0
NGC 4321	SAB(s)bc	7.4×6.3	20.0
NGC 4450	SA(s)ab	5.2×3.9	20.0
NGC 4536	SAB(rs)bc	7.6×3.2	25.0
NGC 4559	SAB(rs)cd	10.7×4.4	11.6
NGC 4569	SAB(rs)ab	9.5×4.4	20.0
NGC 4579	SAB(rs)b	5.9×4.7	20.0
NGC 4594	SA(s)a	8.7×3.5	13.7
NGC 4625	SAB(rs)m pec	2.2×1.9[d]	9.5
NGC 4631	SB(s)d	15.5×2.7	9.0
NGC 4725	SAB(r)ab pec	10.7×7.6	17.1
NGC 4736	(R)SA(r)ab	11.2×9.1	5.3
NGC 4826	(R)SA(rs)ab	10.0×5.4	5.6
NGC 5033	SA(s)c	10.7×5.0	13.3
NGC 5055	SA(rs)bc	12.6×7.2	8.2
NGC 5194[f]	SA(s)bc pec	11.2×6.9	8.2
NGC 5398	(R')SB(s)dm pec	2.8×1.7	15.0
NGC 5408	IB(s)m	1.6×0.8[d]	4.5
NGC 5474	SA(s)cd pec	4.8×4.3[d]	6.9
NGC 5713	SAB(rs)bc pec	2.8×2.5	26.6
NGC 5866	$SA0^+$	4.7×1.9	12.5

Table 1 – *continued*

Name	Hubble Type[a]	Size of Optical Disc (arcmin)[a]	Distance (Mpc)[b]
NGC 6822	IB(s)m	15.5×13.5[c]	0.6
NGC 6946	SAB(rs)cd	11.5×9.8[d]	5.5
NGC 7331	SA(s)b	10.5×3.7	15.7
NGC 7552	(R')SB(s)ab	3.4×2.7	22.3
NGC 7793	SA(s)d	9.3×6.3	3.2

[a] These data are taken from RC3. The optical disc is the size of the D_{25} isophote.
[b] These data are taken from Kennicutt et al. (2003). The distances are calculated using H_0=70 km s^{-1} Mpc^{-1} and the systematic velocities in the Nearby Galaxies Catalog (Tully 1988). Objects in the Virgo Cluster were set to a distance of 20 Mpc, and objects in the M81 Group were set to a distance of 3.5 Mpc.
[c] Significant dust emission is detected outside the optical discs of these galaxies. Morphological parameters were therefore measured in the larger regions described in Table 3. See Section 2.3 for more details.
[d] RC3 does not provide position angles for the major axes of these galaxies, so morphological parameters are measured within circular regions with radii equal to the length of the major axes. See Section 2.3 for more details.
[e] The optical disk of NGC 1097A is excluded from the analysis.
[f] A 2 arcmin region centered on NGC 5195 is excluded from the analysis.

Table 2. Basic Properties of the Serendipitous Sample Galaxies

Name	Hubble Type[a]	Size of Optical Disc (arcmin)[a]	Distance (Mpc)[b]
IC 3583	IBm	2.2×1.1	20.0
NGC 586	SA(s)a	1.6×0.8	28.9
NGC 1317	SAB(r)a	2.8×2.4	25.7
NGC 1510	SA0 pec	1.3×0.7	11.2
NGC 3185	(R)SB(r)a	2.3×1.6	16.4
NGC 3187	SB(s)c pec	3.0×1.3[c]	21.4
NGC 4533	SAd	2.1×0.4	23.9
NGC 4618	SB(rs)m	4.2×3.4	8.6

[a] These data are taken from RC3. The optical disc is given as the major and minor axes of the D_25 isophote.
[b] To maintain consistency with Kennicutt et al. (2003), the distances are calculated using H_0=70 km s^{-1} Mpc^{-1} and the systematic velocities in either the Nearby Galaxies Catalog (Tully 1988) or, if those velocities were not available, the equivalent velocities from RC3. IC 3583 was set at the distance used by Kennicutt et al. for the Virgo Cluster (20 Mpc).
[c] RC3 does not provide a position angle for the major axis of NGC 3187, so morphological parameters are measured within a circular region with a radius equal to the length of the major axes. See Section 2.3 for more details.

$\times$ 5 arcmin individual frames taken in either a mosaic or a single field dither pattern. The 24 μm MIPS observations comprise two scan maps for each target. Each object is observed twice in each wave band so as to identify and remove transient phenomena, particularly asteroids. The FWHM of the PSFs, as stated in the Spitzer Observer's Manual (*Spitzer* Science Center 2006)[11], are 1.6 arcsec at 3.6 μm and 6 arcsec at 24 μm. Details on the observations can be found in the documentation for the SINGS fourth data delivery (SINGS Team 2006)[12].

The IRAC data are processed using a SINGS IRAC pipeline which combines multiple frames of data using a drizzle technique. A description of the technique is presented in Regan et al. (2006). The MIPS data were processed using the MIPS Data Analysis Tools version 3.06 (Gordon et al. 2005) along with additional tools to remove zodiacal light emission in the 24 μm data. Additional details are presented in Bendo et al. (2006). Note that the plate scales of the 24 μm data used in this paper are 1.5 arcsec. Full details are available in the SINGS documentation for the fourth data delivery (SINGS Team 2006).

In the NGC 6822, some diffuse emission from the galaxy may have been subtracted by the software that subtracts the zodiacal light emission from the 24 μm data. Although this effect has not been quantified, we expect the 24 μm emission in NGC 6822 to be dominated by bright, compact sources. We therefore still include NGC 6822 in this analysis, but the results from the 24 μm data should be interpreted cautiously.

2.3 Definitions of Morphological Parameters

Five quantities are used to define the infrared morphologies of these galaxies.

The first parameter used is the concentration parameter. The parameter is given by Bershady et al. (2000), Conselice (2003), and Lotz et al. (2004) as

$$C = 5 \log \left(\frac{r_{80}}{r_{20}} \right) \quad (1)$$

where r_{80} and r_{20} are the radii of the circles that contain 80% and 20% of the total light, respectively. The total light from these galaxies is measured within the optical disks defined by RC3; more details are given later in this section. The centres of the circles for these measurements were chosen to match the centres of the galaxies given in RC3. The uncertainties for C are calculated assuming uncertainties of 1 pixel (1.5 arcsec) in the individual radii, which also effectively accounts for uncertainties related to the correspondence between the centre positions given by RC3 and the true centres of the galaxies in these images. This parameter is generally used to indicate the central concentration of the light, although the form of the parameter used here is really a measure of the concentration of the central 20% of the light. A high value of C indicates that the emission originates primarily from near the centre, whereas a low value indicates that most of the emission is extended.

Lotz et al. (2004) also suggested using the normalized second order moment of the brightest 20% of the emission to indicate the central concentration of light. The unnormalized second order moment of the light is given as

$$M = \sum_{i,j} f(i,j) r(i,j)^2 \quad (2)$$

where $f(i,j)$ is the value of pixel i,j and $r(i,j)$ is the distance from the centre of the target (which is set to the posi-

[11] http://ssc.spitzer.caltech.edu/documents/som/

[12] Available at http://ssc.spitzer.caltech.edu/legacy/singshistory.html

Table 3. Elliptical Measurement Regions Used for DDO 53 and NGC 6822

Name	Centre (J2000) R.A.[a]	Dec.[a]	Major Axis (arcmin)	Minor Axis (arcmin)	Position Angle[b]
DDO 53	08 34 07.2	+66 10 54	2.0	2.0	0°
NGC 6822	19 44 56.6	-14 47 21	27.0	15.0	160°

[a] These are the centres of the optical discs given in RC3.
[b] The position angle is measured in degrees from north through east.

tion given in RC3) to pixel i, j. The normalized second order moment of the brightest 20% of the emission is given by

$$\overline{M}_{20} = \log\left(\frac{M_{20}}{M_{tot}}\right) \quad (3)$$

where M_{20} is the moment of the pixels that constitute the brightest 20% of the emission and M_{tot} is the moment of all the pixels. (Note that the symbols used here are slightly different than what is used in Lotz et al. (2004).) This value is always negative; lower (more negative) values indicate that the emission is more centralized, and higher (less negative) values indicate that the emission is extended. Lotz et al. (2004) suggested using $\overline{M}_{20}$ as an alternative to the central concentration parameter C used by Bershady et al. (2000) and Conselice (2003) because $\overline{M}_{20}$ is weighted towards the most luminous regions. The $\overline{M}_{20}$ parameter measured for some sources (mainly point-like sources) may change by $\sim$ 5% or more if the in the central position is altered by 1 pixel (1.5 arcsec), although the variations are relatively small for most of the galaxies in the sample. Nonetheless, we used a rigorous process described in Appendix A to find the central position used for measuring $\overline{M}_{20}$.

Also of interest is how the infrared light is concentrated compared to the optical light. To do this, we define the normalized effective radius of the light to be

$$\overline{R}_{eff} = \frac{R_{IR\ eff}}{R_{opt}} \quad (4)$$

. $R_{IR\ eff}$ is the semi-major axis of the ellipse (with the same centre, orientation, and ellipticity of the optical disc given in RC3) that contains half of the light in the individual infrared wave band that was measured within the optical disk defined by RC3. R_{opt} is the optical semi-major axis from RC3. This parameter indicates how the dust is distributed relative to the stars in the galaxy. High $\overline{R}_{eff}$ values indicate that the infrared emission is extended compared to the starlight; low $\overline{R}_{eff}$ values indicate that the infrared emission originates primarily from the nuclei of the galaxies. We use the logarithm of $\overline{R}_{eff}$ in this analysis. As for C, the uncertainties for $\overline{R}_{eff}$ are calculated assuming an uncertainties of 1 pixel (1.5 arcsec) in $R_{IR\ eff}$, which also accounts for uncertainties in the centre positions of the galaxies.

The asymmetry in an image can be measured by subtracting an image rotated 180° from the original image. This is given by Abraham et al. (1996) and Conselice (2003) as

$$A = \frac{\sum_{i,j} |f(i,j) - f_{180}(i,j)|}{\sum_{i,j} |f(i,j)|} \quad (5)$$

where $f(i,j)$ is the value of pixel i, j and $f_{180}(i,j)$ is the value of pixel i, j in the image that has been rotated 180° around the centre of the galaxy. Higher values of A indicate that more emission originates from asymmetric structures. Unlike the other parameters used in this analysis, the asymmetry parameter may be highly sensitive to errors in the centre of rotation. We describe the process used to identify the centre or rotation in Appendix A.

We use the Gini coefficient as defined in Lotz et al. (2004) to determine the smoothness or peakedness of the image. (The smoothing parameter S defined by Conselice (2003) relies too heavily on arbitrary choices concerning a smoothing width. Moreover, it is sensitive to the diameter of the galaxy.) To calculate the Gini coefficient, the sky-subtracted pixels must first be ordered from the lowest absolute pixel value to the highest absolute pixel value. The Gini coefficient is then calculated using

$$G = \frac{1}{\overline{|f|} n(n-1)} \sum_{i=1}^{n} (2i - n - 1)|f(i)| \quad (6)$$

where $\overline{|f|}$ is the average absolute pixel value, n is the number of pixels, and $f(i)$ is the value of pixel i after the pixels are reordered by brightness. A high value of G indicates that emission is concentrated in one or a few peaks, whereas a low value of G indicates smooth emission.

The parameters are measured in both the 24 μm data in its native 6 arcsec resolution and in the 3.6 μm data with PSFs that are matched to the PSFs of the 24 μm data. This is done by convolving the 3.6 μm images with the convolution kernels of K. D. Gordon, which not only degrade the resolution of the data but also match the PSF of the 3.6 μm data to the PSF of the 24 μm data[13]. The convolved 3.6 μm data were also rebinned into 1.5 arcsec square pixels to match the pixel scale of the 24 μm data, and the measurements are performed in the same regions used for the 24 μm data. The convolution and rebinning of the 3.6 μm data ensures that resolution and pixelation effects do not create biases when the images are compared to the 24 μm images.

In both the 3.6 and 24 μm data, the parameters are measured within the optical discs of the galaxies as defined in RC3. Note that, if RC3 does not list the ratio of the ellipse's axes or the position angle of the major axis, the measurements are made within a circular region with a diameter equal to the optical diameter listed in RC3. This is only the case for a few galaxies that appear to be close to circular (such as the face-on spiral galaxy NGC 3938) or that have ill-defined shapes (such as Ho I). In many of the 3.6 μm and most of the 24 μm images used in this paper, the surface brightness drops below 3σ detection levels near or inside the optical discs of the galaxies, and foreground

[13] The kernels are available at http://dirty.as.arizona.edu/~kgordon/mips/conv_psfs/conv_psfs.html.

Table 4. Morphological Parameters Measured in a Model Image of the 24 μm PSF

Parameter	Value
C	3.22
$\overline{M}_{20}$	-2.72
A	0.080
G	0.94

stars become the dominant source of emission outside the optical disc in the 3.6 μm images, so inclusion of emission outside the optical disc will only add noise. Exceptions are made for DDO 53 and NGC 6822, where the dust emission clearly extends beyond the galaxies' optical discs. In these cases, the measurements were made in the elliptical regions that are listed in Table 3, which are larger than the optical discs given in RC3.

Note that, while we use of the optical disks defined in RC3 as the regions in which we measure the morphological parameters, Conselice (2003) and Lotz et al. (2004) define the measurement regions using the Petrosian radius. We used the RC3 optical disks instead mainly because we wanted to include the entire area within the optical disks of the sample galaxies when measuring these parameters at 24 μm, whereas areas based on the Petrosian radius may exclude part of the optical disks of some galaxies with 24 μm emission. Moreover, using the optical disks allowed for measuring the same regions in both the 3.6 and 24 μm optical disks. Since the spatial extent of the 3.6 and 24 μm emission may vary within individual galaxies, the Petrosian radii and measurement regions based on the Petrosian radii may vary as well. Furthermore, the galaxies in our sample are all located nearby, so the problems described by Conselice et al. (2000) in defining optical disks and in accounting for redshift and evolution effects (which were part of the justification for using regions based on Petrosian radii) are not as important for our analysis.

Additional sources that fall within the measurement regions (such as foreground stars and companion galaxies) will make the galaxies appear unusually extended and asymmetric in this analysis. Therefore, these sources need to be masked out before measurements are made. Bright foreground stars, identified by eye as unresolved sources with relatively high (generally $\gtrsim$5) 3.6/24 μm flux density ratios, were masked out of the 3.6 μm data and, in a few cases, the 24 μm data. Additionally, a 2 arcmin diameter circular region at the centre of NGC 5195 was excluded from the optical disc of NGC 5194, and NGC 1097A was masked out in the image of NGC 1097.

For reference, the C, $\overline{M}_{20}$, A, and G morphological parameters were measured within a 4 arcmin diameter circular region in a model image of the 24 μm PSF created with STinyTim [14], a PSF simulator designed for *Spitzer* (Krist 2002). The parameters are listed in Table 4. Note that the $\overline{M}_{20}$ and G parameters may vary by $\sim$ 10% if the aperture is increased to 6 arcmin or decreased to 2 arcmin. The C and A parameters, however, do not vary significantly with the diameter of the measurement region. Also note that, in observations of completely unresolved sources, much of the extended structure of the PSF would not be detectable above the background noise, which could change some of the measured parameters, particularly the $\overline{M}_{20}$ and G parameters.

[14] Available from http://ssc.spitzer.caltech.edu/archanaly/contributed/browse.html.

3 ROBUSTNESS TESTS OF THE MORPHOLOGICAL PARAMETERS

Before using the morphological parameters of the 24 μm data to examine morphological trends within the sample, we performed a couple of tests. We first determine how the morphological parameters depend on distance. Next, we determine how the morphological parameters depend on galaxy inclination.

3.1 Dependence of Morphological Parameters on Distance

The galaxies in this sample are not distributed homogeneously with respect to distance. The more distant galaxies tend to be early-type spiral and elliptical galaxies, whereas the nearby galaxies tend to be late-type spiral and irregular galaxies. Moreover, the distant galaxies tend to be relatively unusual objects that were chosen to completely sample the colour-morphology-luminosity space of nearby galaxies. Therefore, we must test how the morphological parameters vary with distance so as to disentangle distance-related effects from true variations in the morphologies related to Hubble-type.

To perform this test, we used the 3.6 and 24 μm images of all galaxies in the sample within 6 Mpc that have optical diameters of at least 10 arcmin except for NGC 6822. This subsample contains 6 galaxies ranging from Sab to Sm. We smoothed and rebinned the images to simulate what the galaxies would look like at a distance of 30 Mpc (approximately the maximum distance for the galaxies in the SINGS sample) in images with the same resolution and pixel scale of the 24 μm images. At a distance of 30 Mpc, all galaxies in the test subsample are still larger than 1 arcmin and are therefore comparable to the most distant galaxies in the sample. (NGC 6822, which is the closest galaxy in the SINGS sample, would have an angular size of $\sim$ 30 arcsec at a distance of 30 Mpc. This is smaller than any of the galaxies in this paper's sample and also poorly resolved at the resolution of the 24 μm data.)

A comparison between the morphological parameters measured in these smoothed images and the parameters measured in the original images is presented in Tables 5 and 6. From these numbers, it can be seen that the C, $\log(\overline{R}_{eff})$, and G are all relatively invariant with distance in both wave bands. The $\overline{M}_{20}$ parameter only varies $\sim$ 20% in both wave bands for most galaxies, although it does increase by a factor of $\sim$ 2 for the 3.6 μm image of NGC 4236; we will simply note these limitations in the analysis rather than develop a correction function. The 3.6 μm A parameter does not strongly vary except for the irregular galaxies IC 2574 and NGC 4236. Again, we will simply note that the 3.6 μm A

Table 5. Comparison of 3.6 μm Morphological Parameters Measured in Original Images and Images Simulated to Represent 30 Mpc Distances

Name	Distance (Mpc)[a]	C	$\overline{M}_{20}$	$\log(\overline{R}_{eff})$	A	G
IC 2574	3.5 (orig)	2.57 ± 0.02	-0.888 ± 0.008	-0.518 ± 0.003	0.6885 ± 0.0002	0.44
	30 (sim)	2.82 ± 0.03	-1.170 ± 0.013	-0.510 ± 0.003	0.54 ± 0.03	0.34
NGC 2403	3.5 (orig)	3.38 ± 0.03	-1.198 ± 0.006	-0.781 ± 0.003	0.4510 ± 0.0015	0.71
	30 (sim)	3.24 ± 0.03	-1.357 ± 0.007	-0.754 ± 0.003	0.313 ± 0.012	0.67
NGC 3031	3.5 (orig)	4.18 ± 0.04	-2.37 ± 0.04	-0.932 ± 0.003	0.103 ± 0.004	0.75
	30 (sim)	3.83 ± 0.04	-2.42 ± 0.03	-0.895 ± 0.003	0.10 ± 0.07	0.73
NGC 4236	3.5 (orig)	3.043 ± 0.017	-0.822 ± 0.007	-0.5938 ± 0.0019	0.51575 ± 0.00012	0.38
	30 (sim)	3.46 ± 0.02	-1.69 ± 0.03	-0.5940 ± 0.0019	0.345 ± 0.014	0.38
NGC 4736	5.3 (orig)	4.48 ± 0.14	-2.73 ± 0.03	-1.019 ± 0.010	0.06 ± 0.04	0.87
	30 (sim)	3.12 ± 0.08	-2.25 ± 0.04	-0.945 ± 0.009	0.09 ± 0.10	0.86
NGC 6946	5.5 (orig)	2.85 ± 0.03	-1.194 ± 0.011	-0.390 ± 0.002	0.3956 ± 0.0005	0.58
	30 (sim)	2.80 ± 0.03	-1.130 ± 0.008	-0.369 ± 0.002	0.343 ± 0.007	0.55

[a] The measurements in the original images have distances labelled as (orig). The measurements in the simulated images have distances labelled as (sim).

Table 6. Comparison of 24 μm Morphological Parameters Measured in Original Images and Images Simulated to Represent 30 Mpc Distances

Name	Distance (Mpc)[a]	C	$\overline{M}_{20}$	$\log(\overline{R}_{eff})$	A	G
IC 2574	3.5 (orig)	1.582 ± 0.014	-0.653 ± 0.016	-0.3259 ± 0.0017	1.884 ± 0.005	0.62
	30 (sim)	1.99 ± 0.02	-0.6 ± 0.4	-0.3418 ± 0.0018	1.1 ± 0.4	0.54
NGC 2403	3.5 (orig)	2.53 ± 0.03	-1.138 ± 0.015	-0.925 ± 0.004	1.009 ± 0.0004	0.82
	30 (sim)	2.64 ± 0.03	-1.37 ± 0.014	-0.863 ± 0.004	0.59 ± 0.02	0.80
NGC 3031	3.5 (orig)	2.95 ± 0.02	-1.01 ± 0.02	-0.6818 ± 0.0019	0.763 ± 0.005	0.71
	30 (sim)	2.95 ± 0.03	-1.3 ± 0.3	-0.6676 ± 0.0019	0.38 ± 0.04	0.69
NGC 4236	3.5 (orig)	1.414 ± 0.013	-0.896 ± 0.014	-0.600 ± 0.002	1.786 ± 0.003	0.67
	30 (sim)	1.858 ± 0.016	-0.8 ± 0.5	-0.5618 ± 0.0018	0.95 ± 0.16	0.66
NGC 4736	5.3 (orig)	2.96 ± 0.10	-1.661 ± 0.017	-0.971 ± 0.009	0.30 ± 0.02	0.89
	30 (sim)	2.53 ± 0.08	-2.07 ± 0.06	-0.899 ± 0.008	0.15 ± 0.02	0.66
NGC 6946	5.5 (orig)	5.82 ± 0.13	-2.02 ± 0.11	-0.525 ± 0.003	0.656 ± 0.014	0.78
	30 (sim)	4.42 ± 0.07	-2.47 ± 0.03	-0.510 ± 0.003	0.453 ± 0.019	0.74

[a] The measurements in the original images have distances labelled as (orig). The measurements in the simulated images have distances labelled as (sim).

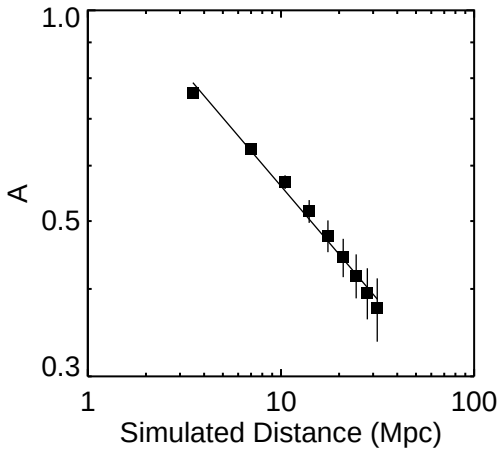

Figure 1. Variations in the A parameter measured in images of NGC 3031 simulated to represent the galaxy's appearance at distances between 3.5 and $\sim$ 30 Mpc (see Section 3.1). The line represents the best-fitting power law, which has a slope of -0.30.

parameter for the irregular galaxies may be highly uncertain, but we will skip applying a correction factor for this analysis. The 24 μm A parameter, however, decreases by approximately a factor of 2 for all galaxies. This indicates that the 24 μm A parameter is dependent on distance for all galaxies and that a correction needs to be applied.

To find the correction for the 24 μm A parameter, we produced simulated images of each test subsample galaxies at several artificial distances between their actual distance and 30 Mpc and measured the A parameter. We empirically examined the data and determined that the function that best describes the relation between A and distance is a power law. We used a least-squares fit to the data to find the index of the power law that describes A as a function of simulated distance for each galaxy. An example using NGC 3031 is shown in Figure 1. Afterwards, we averaged the power law indices from the fits to all galaxies. The result is

$$A \propto d^{-0.26 \pm 0.03} \quad (7)$$

To correct the 24 μm A parameters, we will adjust all measured A values to their equivalent at a distance of 10 Mpc (the approximate median distance of the galaxies in this sample) using the equation

Table 7. Comparison of 3.6 μm Morphological Parameters Measured in Original Images and Images Simulated to Various Inclinations

Name	Inclination[a]	C	$\overline{M}_{20}$	$\log(\overline{R}_{eff})$	A	G
NGC 628	0° (orig)	2.97 ± 0.04	-1.592 ± 0.017	-0.482 ± 0.017	0.273 ± 0.004	0.65
	40° (sim)	2.97 ± 0.04	-1.574 ± 0.019	-0.60 ± 0.02	0.2736 ± 0.0015	0.65
	80° (sim)	3.78 ± 0.07	-1.520 ± 0.011	-1.04 ± 0.06	0.2750 ± 0.0005	0.64
NGC 3184	0° (orig)	2.43 ± 0.04	-1.63 ± 0.02	-0.386 ± 0.019	0.241 ± 0.002	0.55
	40° (sim)	2.48 ± 0.04	-1.68 ± 0.02	-0.50 ± 0.02	0.241 ± 0.002	0.55
	80° (sim)	3.43 ± 0.08	-1.94 ± 0.03	-0.94 ± 0.07	0.2419 ± 0.0006	0.55
NGC 3938	0° (orig)	2.96 ± 0.07	-2.03 ± 0.03	-0.49 ± 0.03	0.214 ± 0.004	0.63
	40° (sim)	2.91 ± 0.08	-2.03 ± 0.03	-0.60 ± 0.04	0.214 ± 0.004	0.63
	80° (sim)	3.63 ± 0.14	-2.09 ± 0.03	-1.03 ± 0.12	0.230 ± 0.004	0.63

[a] The measurements in the original images have inclinations labelled as 0° (orig). The measurements in the simulated images have inclinations labelled as (sim).

Table 8. Comparison of 24 μm Morphological Parameters Measured in Original Images and Images Simulated to Various Inclinations

Name	Inclination[a]	C	$\overline{M}_{20}$	$\log(\overline{R}_{eff})$	A	G
NGC 628	0° (orig)	1.94 ± 0.03	-0.845 ± 0.014	-0.446 ± 0.015	0.9016 ± 0.0007	0.73
	40° (sim)	1.96 ± 0.03	-0.884 ± 0.015	-0.58 ± 0.02	0.9002 ± 0.0010	0.73
	80° (sim)	2.76 ± 0.05	-1.02 ± 0.02	-1.01 ± 0.06	0.841 ± 0.009	0.74
NGC 3184	0° (orig)	2.02 ± 0.04	-0.997 ± 0.018	-0.40 ± 0.02	0.728 ± 0.006	0.68
	40° (sim)	2.16 ± 0.04	-1.021 ± 0.019	-0.51 ± 0.03	0.723 ± 0.010	0.68
	80° (sim)	3.44 ± 0.09	-1.09 ± 0.06	-0.94 ± 0.07	0.688 ± 0.010	0.68
NGC 3938	0° (orig)	2.37 ± 0.06	-0.858 ± 0.008	-0.47 ± 0.03	0.6574 ± 0.0006	0.71
	40° (sim)	2.39 ± 0.06	-0.817 ± 0.008	-0.59 ± 0.04	0.6553 ± 0.0009	0.71
	80° (sim)	3.22 ± 0.11	-0.694 ± 0.007	-0.97 ± 0.10	0.612 ± 0.008	0.71

[a] The measurements in the original images have inclinations labelled as 0° (orig). The measurements in the simulated images have inclinations labelled as (sim).

$$A_{corrected} = 0.55 A_{observed} d^{0.30} \quad (8)$$

where d is in Mpc. This equation may only be applicable to the 24 μm data, as the power law probably varies with wave band and resolution.

This analysis does indicate that the A and $\overline{M}_{20}$ parameters may be sensitive to distance in other wave bands that trace either dust or star formation. Therefore, their usefulness at redshifts higher than those in this sample may be questionable. As is also discussed by (Lotz et al. 2004), simulated high-redshift images of nearby galaxies are needed to compare to observed high-redshift galaxies. The distance-sensitivity of the two parameters also implies that they are dependent on the angular resolution at which the galaxies are observed. Therefore, to accurately compare parameters measured within images of two different wave bands, the images must have matching resolutions.

3.2 Dependence of Morphological Parameters on Inclination

Since the galaxies in this sample exhibit a wide range of inclinations and since galaxies' appearance change when viewed edge-on, we simulated the effects of inclining a galaxy between 0° and 80° using NGC 628, NGC 3184, and NGC 3938, which have minor/major axis ratios of 0.9 or higher and optical diameters greater than 5 arcmin. In this analysis, these galaxies are treated as having inclinations of 0°, although the axis ratios may imply a slight inclination. The simulated inclinations were performed simply by projecting the images onto a plane tilted to the desired angle. For this analysis, the emission is assumed to be infinitely thin, although we note that significant stellar emission may extend outside the plane of S0 and early-type spiral galaxies.

A comparison between the 3.6 and 24 μm morphological parameters measured in the original images and images with simulated inclinations of 40° and 80° is shown in Table 7 and 8. For this section alone, the measurements region is treated as circular in the original images. In the images with simulated inclinations, the ratio of the axes of the measurement region is set to the cosine of the inclination angle. The A, $\overline{M}_{20}$, and G parameters all vary less than $\sim 20\%$ between the original and simulated images, but the comparison demonstrates that C and $\log(\overline{R}_{eff})$ for both wave bands are sensitive to inclination effects. These will need to be corrected to deal with these inclination effects.

We derive relations for the corrections needed to be applied to these parameters by measuring the C and $\log(\overline{R}_{eff})$ parameters measured in the 3.6 and 24 μm images simulated with inclinations between 0° and 85°. For the C parameter, we empirically determined that it varies as a function of a constant added to θ^4, where θ is the inclination angle in degrees. The $\log(\overline{R}_{eff})$ parameter was found to vary as a function of $cos(\theta)$. These functions were fit to C and $\log(\overline{R}_{eff})$ for each galaxy in each wave band, and then the median and uncertainty for the resulting coefficients were calculated to give the following correction functions:

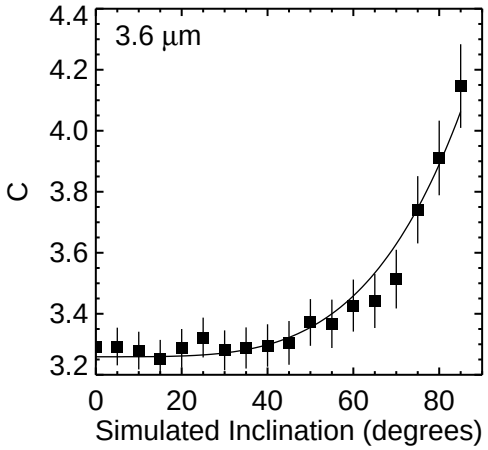

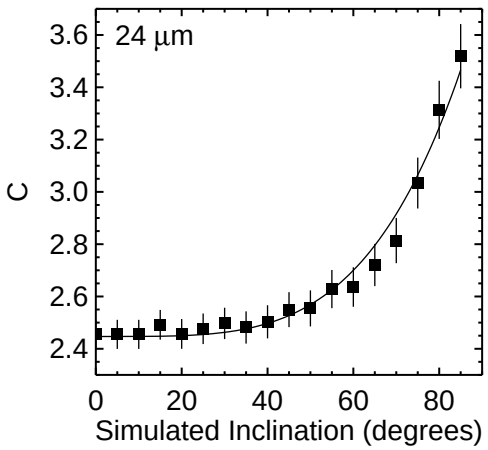

Figure 2. Variations in the C parameter measured in images of NGC 3938 simulated to represent the galaxy's appearance at various inclinations (see Section 3.2). The lines represent the best-fitting function.

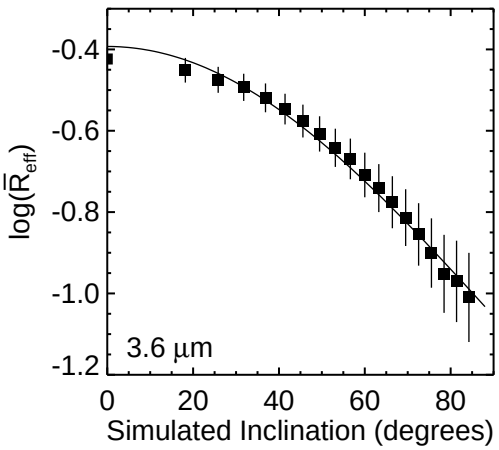

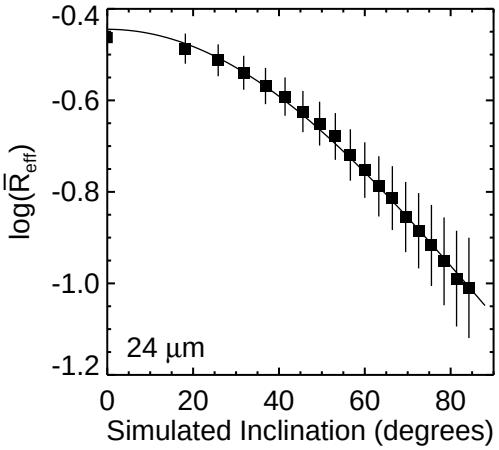

Figure 3. Variations in the $\log(\overline{R}_{eff})$ parameter measured in images of NGC 3938 simulated to represent the galaxy's appearance at various inclinations (see Section 3.2). The lines represent the best-fitting function.

$$C_{corrected} = C_{original} - (2.0 \pm 0.3) \times 10^{-8}\theta^4 \quad (9)$$

$$\log(\overline{R}_{eff})_{corrected} = \log(\overline{R}_{eff})_{original} + (0.675 \pm 0.012)(1 - \cos(\theta)) \quad (10)$$

The values for $C_{corrected}$ and $\log(\overline{R}_{eff})_{corrected}$ are the parameters that would be measured if the galaxies were viewed face-on. Example fits are shown for NGC 3938 in Figures 2 and 3. Note that the variations in each wave band are statistically similar.

The inclination-related corrections are only applied to disc galaxies (S0-Sd galaxies). To apply these corrections, the inclination is calculated using

$$\theta = \cos^{-1}\left(\left(\frac{(\frac{r_{minor}}{r_{major}})^2 - q_o^2}{1 - q_o^2}\right)^{0.5}\right) \quad (11)$$

where r_{minor} is the optical semiminor axis, r_{major} is the optical semimajor axis, and q_o is the intrinsic optical axial ratio, which is set to 0.20. NGC 3190, NGC 4631, and NGC 5866 are viewed close to edge-on, so the inclination is set to 90° for these galaxies.

Because the correction was calculated assuming that the stellar and 24 μm emission was infinitely thin (geometrically and optically), the corrections may be inaccurate for the 3.6 μm parameters of some nearly edge-on early-type spiral and S0 galaxies. However, we anticipate that the 24 μm emission should originate mostly from a thin disc, so the corrections should be accurate for the 24 μm parameters. The 3.6 μm stellar emission from late-type galaxies should also originate from a relatively thin disc, so the corrections for the 3.6 μm emission for these galaxies should also be fairly accurate.

This analysis demonstrates that the C parameter has the added disadvantage over the $\overline{M}_{20}$ parameter of being more sensitive to inclination effects. Given that $\overline{M}_{20}$ is also a more sensitive concentration parameter (Lotz et al. 2004), it should be used instead of C as a concentration parameter. The C parameter is still included here so as to allow

Table 9. Morphological Parameters Measured in 3.6 μm Data

Name	C^a	$\overline{M}_{20}$	$\overline{R}_{eff}{}^b$	$\log(\overline{R}_{eff})^b$	A	G
DDO 53	2.52 ± 0.11	-0.695 ± 0.010	0.726 ± 0.016	-0.139 ± 0.010	1.1360 ± 0.0004	0.56
Ho I	1.85 ± 0.05	-0.748 ± 0.008	0.592 ± 0.007	-0.228 ± 0.005	0.7670 ± 0.0008	0.41
Ho II	2.44 ± 0.03	-0.738 ± 0.007	0.415 ± 0.003	-0.381 ± 0.003	0.7823 ± 0.0005	0.54
IC 2574	2.57 ± 0.02	-0.888 ± 0.008	0.3034 ± 0.0019	-0.518 ± 0.003	0.6885 ± 0.0002	0.44
IC 3583	1.67 ± 0.13	-0.884 ± 0.006	0.251 ± 0.011	-0.60 ± 0.02	1.002 ± 0.008	0.59
IC 4710	2.07 ± 0.06	-0.883 ± 0.004	0.413 ± 0.007	-0.384 ± 0.007	0.512 ± 0.002	0.41
Mrk 33	2.8 ± 0.4	-2.02 ± 0.03	0.30 ± 0.03	-0.52 ± 0.04	0.10 ± 0.09	0.67
NGC 24	2.18 ± 0.10	-1.88 ± 0.02	0.711 ± 0.004	-0.148 ± 0.003	0.206 ± 0.007	0.54
NGC 337	2.28 ± 0.13	-1.649 ± 0.017	0.460 ± 0.009	-0.337 ± 0.008	0.2799 ± 0.0010	0.63
NGC 628	2.95 ± 0.04	-1.573 ± 0.019	0.358 ± 0.002	-0.446 ± 0.003	0.266 ± 0.003	0.63
NGC 855	3.2 ± 0.2	-2.136 ± 0.019	0.124 ± 0.010	-0.91 ± 0.03	0.10 ± 0.02	0.59
NGC 925	2.82 ± 0.04	-1.324 ± 0.009	0.501 ± 0.002	-0.301 ± 0.002	0.391 ± 0.004	0.55
NGC 1097	4.78 ± 0.12	-2.78 ± 0.02	0.264 ± 0.003	-0.579 ± 0.004	0.1932 ± 0.0011	0.71
NGC 1266	3.1 ± 0.3	-2.15 ± 0.02	0.545 ± 0.016	-0.263 ± 0.013	0.093 ± 0.003	0.64
NGC 1291	4.99 ± 0.09	-2.87 ± 0.03	0.282 ± 0.003	-0.549 ± 0.004	0.09 ± 0.02	0.65
NGC 1316	4.55 ± 0.08	-2.77 ± 0.03	0.245 ± 0.002	-0.612 ± 0.004	0.091 ± 0.010	0.69
NGC 1317	3.9 ± 0.2	-2.39 ± 0.02	0.313 ± 0.009	-0.504 ± 0.013	0.0628 ± 0.0014	0.60
NGC 1377	3.0 ± 0.4	-2.28 ± 0.03	0.321 ± 0.014	-0.494 ± 0.019	0.10 ± 0.05	0.68
NGC 1482	3.1 ± 0.4	-2.32 ± 0.03	0.209 ± 0.010	-0.68 ± 0.02	0.11 ± 0.05	0.81
NGC 1510	2.6 ± 0.3	-2.00 ± 0.03	0.438 ± 0.019	-0.358 ± 0.019	0.07 ± 0.05	0.54
NGC 1512	3.93 ± 0.10	-2.58 ± 0.03	0.313 ± 0.003	-0.504 ± 0.004	0.139 ± 0.014	0.71
NGC 1566	3.57 ± 0.08	-2.41 ± 0.04	0.273 ± 0.003	-0.564 ± 0.005	0.191 ± 0.006	0.72
NGC 1705	3.3 ± 0.2	-2.20 ± 0.04	0.360 ± 0.013	-0.444 ± 0.016	0.37 ± 0.02	0.60
NGC 2403	3.16 ± 0.03	-1.198 ± 0.006	0.3406 ± 0.0011	-0.4678 ± 0.0015	0.4510 ± 0.0015	0.71
NGC 2798	2.8 ± 0.4	-2.33 ± 0.04	0.248 ± 0.010	-0.606 ± 0.017	0.14 ± 0.07	0.76
NGC 2841	3.37 ± 0.09	-2.44 ± 0.03	0.354 ± 0.003	-0.451 ± 0.004	0.0618 ± 0.0006	0.64
NGC 2915	2.55 ± 0.17	-1.74 ± 0.03	0.262 ± 0.013	-0.58 ± 0.02	0.33 ± 0.02	0.44
NGC 2976	1.93 ± 0.06	-1.045 ± 0.010	0.586 ± 0.004	-0.232 ± 0.003	0.181 ± 0.002	0.54
NGC 3031	3.91 ± 0.04	-2.37 ± 0.04	0.2565 ± 0.0009	-0.5910 ± 0.0016	0.103 ± 0.004	0.75
NGC 3049	3.06 ± 0.19	-2.07 ± 0.02	0.498 ± 0.011	-0.303 ± 0.010	0.12 ± 0.03	0.50
NGC 3184	2.40 ± 0.04	-1.62 ± 0.02	0.440 ± 0.003	-0.357 ± 0.003	0.239 ± 0.002	0.53
NGC 3185	3.03 ± 0.19	-2.18 ± 0.03	0.471 ± 0.011	-0.327 ± 0.010	0.11 ± 0.03	0.56
NGC 3187	2.71 ± 0.12	-1.713 ± 0.015	0.904 ± 0.008	-0.044 ± 0.004	0.3399 ± 0.0006	0.65
NGC 3190	2.5 ± 0.2	-2.48 ± 0.03	0.434 ± 0.006	-0.363 ± 0.006	0.116 ± 0.015	0.71
NGC 3198	2.54 ± 0.07	-1.73 ± 0.03	0.352 ± 0.003	-0.453 ± 0.004	0.153 ± 0.003	0.67
NGC 3265	2.6 ± 0.4	-1.99 ± 0.03	0.194 ± 0.019	-0.71 ± 0.04	0.10 ± 0.05	0.73
NGC 3351	3.97 ± 0.10	-2.57 ± 0.03	0.349 ± 0.003	-0.457 ± 0.004	0.081 ± 0.007	0.64
NGC 3521	3.21 ± 0.08	-2.36 ± 0.03	0.259 ± 0.002	-0.586 ± 0.004	0.086 ± 0.017	0.74
NGC 3621	3.23 ± 0.05	-1.554 ± 0.010	0.339 ± 0.002	-0.470 ± 0.003	0.40076 ± 0.00012	0.72
NGC 3627	2.93 ± 0.07	-2.04 ± 0.04	0.365 ± 0.003	-0.438 ± 0.003	0.290 ± 0.003	0.67
NGC 3773	2.8 ± 0.3	-1.96 ± 0.02	0.38 ± 0.02	-0.42 ± 0.02	0.08 ± 0.05	0.54
NGC 3938	2.95 ± 0.07	-2.03 ± 0.03	0.376 ± 0.005	-0.425 ± 0.005	0.214 ± 0.004	0.63
NGC 4125	4.00 ± 0.14	-2.49 ± 0.03	0.148 ± 0.004	-0.831 ± 0.013	0.06 ± 0.02	0.65
NGC 4236	3.043 ± 0.017	-0.822 ± 0.007	0.2548 ± 0.0011	-0.5938 ± 0.0019	0.51575 ± 0.00012	0.47
NGC 4254	3.13 ± 0.08	-2.10 ± 0.03	0.367 ± 0.005	-0.435 ± 0.006	0.3460 ± 0.0003	0.69
NGC 4321	3.03 ± 0.05	-1.88 ± 0.03	0.412 ± 0.003	-0.385 ± 0.004	0.215 ± 0.007	0.57
NGC 4450	3.50 ± 0.10	-2.32 ± 0.03	0.370 ± 0.005	-0.431 ± 0.006	0.074 ± 0.016	0.61
NGC 4533	1.8 ± 0.2	-1.83 ± 0.03	0.796 ± 0.012	-0.099 ± 0.007	0.07 ± 0.02	0.47
NGC 4536	4.6 ± 0.2	-3.00 ± 0.02	0.249 ± 0.003	-0.604 ± 0.006	0.16 ± 0.03	0.73
NGC 4559	2.69 ± 0.06	-2.06 ± 0.03	0.333 ± 0.002	-0.477 ± 0.003	0.264 ± 0.002	0.69
NGC 4569	3.42 ± 0.08	-2.39 ± 0.06	0.342 ± 0.003	-0.466 ± 0.003	0.162 ± 0.004	0.70
NGC 4579	3.92 ± 0.11	-2.46 ± 0.03	0.338 ± 0.004	-0.471 ± 0.005	0.093 ± 0.004	0.63
NGC 4594	3.18 ± 0.08	-2.33 ± 0.03	0.348 ± 0.003	-0.458 ± 0.004	0.033 ± 0.011	0.65
NGC 4625	2.63 ± 0.16	-1.89 ± 0.02	0.343 ± 0.011	-0.465 ± 0.014	0.4658 ± 0.0017	0.69
NGC 4631	2.68 ± 0.07	-2.063 ± 0.017	0.2368 ± 0.0016	-0.626 ± 0.003	0.416 ± 0.010	0.73
NGC 4725	3.68 ± 0.06	-1.706 ± 0.011	0.342 ± 0.002	-0.466 ± 0.003	0.174 ± 0.018	0.69
NGC 4736	4.45 ± 0.14	-2.73 ± 0.03	0.130 ± 0.002	-0.886 ± 0.007	0.06 ± 0.04	0.87
NGC 4826	3.40 ± 0.08	-2.30 ± 0.03	0.284 ± 0.003	-0.546 ± 0.004	0.4374 ± 0.0006	0.73
NGC 5033	4.32 ± 0.14	-2.81 ± 0.03	0.181 ± 0.002	-0.743 ± 0.006	0.175 ± 0.020	0.78
NGC 5055	3.47 ± 0.06	-2.38 ± 0.03	0.307 ± 0.002	-0.512 ± 0.003	0.112 ± 0.005	0.68

Table 9 – *continued*

Name	C^a	$\overline{M}_{20}$	$\overline{R}_{eff}{}^b$	$\log(\overline{R}_{eff})^b$	A	G
NGC 5194	3.00 ± 0.05	-1.89 ± 0.04	0.439 ± 0.002	-0.358 ± 0.002	0.2517 ± 0.0012	0.62
NGC 5398	2.32 ± 0.10	-1.500 ± 0.012	0.293 ± 0.009	-0.534 ± 0.013	0.265 ± 0.004	0.44
NGC 5408	2.03 ± 0.12	-0.728 ± 0.008	0.555 ± 0.015	-0.256 ± 0.012	0.7188 ± 0.0004	0.48
NGC 5474	2.90 ± 0.07	-1.85 ± 0.04	0.499 ± 0.005	-0.302 ± 0.005	0.943 ± 0.012	0.64
NGC 5713	3.00 ± 0.16	-1.99 ± 0.02	0.292 ± 0.009	-0.534 ± 0.013	0.365 ± 0.011	0.69
NGC 5866	2.18 ± 0.16	-2.295 ± 0.016	0.481 ± 0.005	-0.318 ± 0.005	0.06 ± 0.02	0.68
NGC 6822	2.234 ± 0.011	-0.722 ± 0.005	0.6457 ± 0.0016	-0.1900 ± 0.0011	0.6917 ± 0.0004	0.54
NGC 6946	2.83 ± 0.03	-1.194 ± 0.011	0.519 ± 0.002	-0.2851 ± 0.0018	0.3956 ± 0.0005	0.58
NGC 7331	3.23 ± 0.10	-2.51 ± 0.03	0.326 ± 0.002	-0.486 ± 0.003	0.13068 ± 0.00002	0.74
NGC 7552	4.3 ± 0.3	-2.61 ± 0.02	0.217 ± 0.007	-0.664 ± 0.015	0.131 ± 0.008	0.75
NGC 7793	2.48 ± 0.04	-1.84 ± 0.03	0.496 ± 0.003	-0.305 ± 0.002	0.1890 ± 0.0014	0.52

[a] These data have been corrected for inclination effects using Equation 9.
[b] These data have been corrected for inclination effects using Equation 10.

Table 10. Morphological Parameters Measured in 24 μm Data

Name	C^a	$\overline{M}_{20}$	$\overline{R}_{eff}{}^b$	$\log(\overline{R}_{eff})^b$	A^c	G
DDO 53	4.9 ± 0.4	-2.67 ± 0.03	0.242 ± 0.016	-0.62 ± 0.03	0.70 ± 0.03	0.73
Ho I	1.32 ± 0.04	-1.11 ± 0.10	0.599 ± 0.007	-0.223 ± 0.005	3.28 ± 0.11	0.45
Ho II	2.42 ± 0.04	-0.946 ± 0.012	0.412 ± 0.003	-0.385 ± 0.003	1.456 ± 0.006	0.68
IC 2574	1.582 ± 0.014	-0.653 ± 0.016	0.4722 ± 0.0019	-0.3259 ± 0.0017	1.436 ± 0.005	0.62
IC 3583	2.13 ± 0.15	-1.075 ± 0.013	0.206 ± 0.011	-0.69 ± 0.02	1.586 ± 0.005	0.67
IC 4710	1.80 ± 0.06	-0.927 ± 0.018	0.392 ± 0.007	-0.406 ± 0.008	1.117 ± 0.005	0.58
Mrk 33	2.7 ± 0.6	-2.16 ± 0.08	0.20 ± 0.03	-0.70 ± 0.05	0.239 ± 0.012	0.83
NGC 24	2.02 ± 0.10	-1.30 ± 0.03	0.677 ± 0.004	-0.169 ± 0.003	0.506 ± 0.003	0.64
NGC 337	2.24 ± 0.14	-1.13 ± 0.05	0.429 ± 0.009	-0.368 ± 0.009	1.18 ± 0.03	0.75
NGC 586	1.8 ± 0.2	-1.09 ± 0.02	0.412 ± 0.016	-0.385 ± 0.017	0.289 ± 0.009	0.65
NGC 628	1.91 ± 0.03	-0.835 ± 0.013	0.386 ± 0.002	-0.414 ± 0.003	0.905 ± 0.004	0.72
NGC 855	2.6 ± 0.4	-2.10 ± 0.03	0.067 ± 0.010	-1.18 ± 0.06	0.30 ± 0.03	0.83
NGC 925	2.84 ± 0.04	-0.902 ± 0.011	0.520 ± 0.002	-0.284 ± 0.002	0.993 ± 0.003	0.67
NGC 1097	4.11 ± 0.18	-2.335 ± 0.013	0.068 ± 0.003	-1.166 ± 0.017	0.320 ± 0.003	0.89
NGC 1266	2.7 ± 0.6	-2.39 ± 0.10	0.182 ± 0.016	-0.74 ± 0.04	0.34 ± 0.02	0.89
NGC 1291	5.55 ± 0.09	-1.60 ± 0.05	0.481 ± 0.003	-0.318 ± 0.002	0.842 ± 0.003	0.61
NGC 1316	5.65 ± 0.18	-3.63 ± 0.03	0.141 ± 0.002	-0.852 ± 0.006	1.06 ± 0.04	0.70
NGC 1317	2.43 ± 0.19	-1.700 ± 0.015	0.201 ± 0.009	-0.70 ± 0.02	0.254 ± 0.006	0.80
NGC 1377	2.4 ± 0.6	-2.26 ± 0.08	0.160 ± 0.014	-0.79 ± 0.04	0.25 ± 0.05	0.89
NGC 1482	2.4 ± 0.5	-2.26 ± 0.05	0.147 ± 0.010	-0.83 ± 0.03	0.196 ± 0.014	0.90
NGC 1510	2.6 ± 0.6	-2.06 ± 0.06	0.279 ± 0.019	-0.55 ± 0.03	0.225 ± 0.013	0.83
NGC 1512	4.83 ± 0.18	-2.98 ± 0.02	0.318 ± 0.003	-0.497 ± 0.004	0.62 ± 0.02	0.76
NGC 1566	2.25 ± 0.06	-1.045 ± 0.009	0.273 ± 0.003	-0.564 ± 0.005	0.777 ± 0.018	0.85
NGC 1705	2.06 ± 0.19	-1.289 ± 0.011	0.340 ± 0.013	-0.468 ± 0.017	0.319 ± 0.013	0.72
NGC 2403	2.31 ± 0.03	-1.138 ± 0.015	0.2443 ± 0.0011	-0.612 ± 0.002	0.769 ± 0.002	0.82
NGC 2798	2.5 ± 0.6	-2.31 ± 0.05	0.138 ± 0.010	-0.86 ± 0.03	0.20 ± 0.04	0.90
NGC 2841	1.65 ± 0.04	-1.00 ± 0.02	0.448 ± 0.003	-0.348 ± 0.003	0.2712 ± 0.0010	0.61
NGC 2915	2.8 ± 0.3	-1.503 ± 0.016	0.171 ± 0.013	-0.77 ± 0.03	0.587 ± 0.003	0.67
NGC 2976	1.29 ± 0.05	-0.636 ± 0.009	0.764 ± 0.004	-0.117 ± 0.002	0.5903 ± 0.0011	0.77
NGC 3031	2.68 ± 0.02	-1.01 ± 0.02	0.4560 ± 0.0009	-0.3411 ± 0.0009	0.581 ± 0.005	0.71
NGC 3049	3.3 ± 0.6	-2.48 ± 0.06	0.139 ± 0.011	-0.86 ± 0.04	0.27 ± 0.07	0.85
NGC 3184	2.04 ± 0.04	-0.987 ± 0.018	0.428 ± 0.003	-0.368 ± 0.003	0.691 ± 0.006	0.66
NGC 3185	4.5 ± 0.4	-2.61 ± 0.04	0.199 ± 0.011	-0.70 ± 0.02	0.270 ± 0.015	0.76
NGC 3187	2.27 ± 0.14	-1.408 ± 0.016	0.706 ± 0.008	-0.151 ± 0.005	0.865 ± 0.004	0.75
NGC 3190	2.8 ± 0.2	-2.51 ± 0.04	0.488 ± 0.006	-0.312 ± 0.005	0.4161 ± 0.0012	0.79
NGC 3198	5.0 ± 0.2	-1.41 ± 0.09	0.286 ± 0.003	-0.543 ± 0.004	0.48 ± 0.05	0.80
NGC 3265	2.9 ± 0.6	-2.23 ± 0.05	0.136 ± 0.019	-0.87 ± 0.06	0.15 ± 0.15	0.85
NGC 3351	5.2 ± 0.3	-2.663 ± 0.008	0.074 ± 0.003	-1.13 ± 0.02	0.261 ± 0.018	0.83
NGC 3521	2.15 ± 0.06	-1.248 ± 0.008	0.248 ± 0.002	-0.605 ± 0.004	0.3735 ± 0.0011	0.82
NGC 3621	1.97 ± 0.05	-1.143 ± 0.009	0.278 ± 0.002	-0.556 ± 0.003	0.644 ± 0.009	0.84
NGC 3627	1.12 ± 0.04	-0.920 ± 0.013	0.378 ± 0.003	-0.422 ± 0.003	0.851 ± 0.013	0.83
NGC 3773	2.5 ± 0.5	-2.06 ± 0.05	0.22 ± 0.02	-0.66 ± 0.04	0.21 ± 0.03	0.82

Table 10 – *continued*

Name	C^a	$\overline{M}_{20}$	$\overline{R}_{eff}{}^b$	$\log(\overline{R}_{eff})^b$	A^c	G
NGC 3938	2.36 ± 0.06	-0.857 ± 0.009	0.392 ± 0.005	-0.407 ± 0.005	0.692 ± 0.003	0.71
NGC 4125	4.40 ± 0.16	-2.76 ± 0.03	0.148 ± 0.004	-0.831 ± 0.013	0.868 ± 0.011	0.64
NGC 4236	1.414 ± 0.013	-0.896 ± 0.014	0.2514 ± 0.0011	-0.600 ± 0.002	1.361 ± 0.003	0.67
NGC 4254	2.69 ± 0.07	-1.50 ± 0.02	0.379 ± 0.005	-0.421 ± 0.005	0.756 ± 0.003	0.74
NGC 4321	4.54 ± 0.12	-2.23 ± 0.11	0.344 ± 0.003	-0.464 ± 0.004	0.675 ± 0.005	0.75
NGC 4450	3.62 ± 0.12	-1.98 ± 0.04	0.363 ± 0.005	-0.440 ± 0.006	0.77 ± 0.03	0.65
NGC 4533	1.2 ± 0.2	-1.364 ± 0.012	0.690 ± 0.012	-0.161 ± 0.008	0.298 ± 0.013	0.56
NGC 4536	3.8 ± 0.4	-2.88 ± 0.03	0.077 ± 0.003	-1.112 ± 0.019	0.29 ± 0.08	0.90
NGC 4559	2.48 ± 0.06	-1.075 ± 0.010	0.295 ± 0.002	-0.529 ± 0.003	0.8205 ± 0.0009	0.77
NGC 4569	5.3 ± 0.4	-3.278 ± 0.018	0.142 ± 0.003	-0.848 ± 0.008	0.56 ± 0.04	0.89
NGC 4579	4.10 ± 0.15	-1.803 ± 0.018	0.362 ± 0.004	-0.441 ± 0.005	0.57 ± 0.02	0.74
NGC 4594	3.54 ± 0.08	-1.17 ± 0.05	0.433 ± 0.003	-0.363 ± 0.003	0.284 ± 0.019	0.72
NGC 4618	2.26 ± 0.06	-1.075 ± 0.018	0.342 ± 0.006	-0.466 ± 0.008	0.8625 ± 0.0011	0.64
NGC 4625	2.44 ± 0.16	-1.564 ± 0.015	0.297 ± 0.011	-0.527 ± 0.017	0.688 ± 0.007	0.74
NGC 4631	2.77 ± 0.07	-1.817 ± 0.016	0.1757 ± 0.0016	-0.755 ± 0.004	0.67 ± 0.02	0.81
NGC 4725	1.39 ± 0.02	-0.98 ± 0.03	0.455 ± 0.002	-0.342 ± 0.002	0.9781 ± 0.0016	0.67
NGC 4736	2.93 ± 0.10	-1.661 ± 0.017	0.145 ± 0.002	-0.839 ± 0.007	0.25 ± 0.02	0.89
NGC 4826	2.80 ± 0.16	-2.172 ± 0.015	0.113 ± 0.003	-0.948 ± 0.010	0.9207 ± 0.0009	0.91
NGC 5033	3.95 ± 0.12	-2.45 ± 0.03	0.175 ± 0.002	-0.757 ± 0.006	0.5065 ± 0.0005	0.82
NGC 5055	2.78 ± 0.05	-1.240 ± 0.015	0.319 ± 0.002	-0.496 ± 0.003	0.4326 ± 0.0008	0.78
NGC 5194	3.02 ± 0.05	-1.246 ± 0.011	0.443 ± 0.002	-0.354 ± 0.002	0.5603 ± 0.0009	0.73
NGC 5398	0.77 ± 0.08	-0.78 ± 0.03	0.328 ± 0.009	-0.484 ± 0.012	1.9184 ± 0.0019	0.85
NGC 5408	0.69 ± 0.08	-0.64 ± 0.03	0.647 ± 0.015	-0.189 ± 0.010	1.4430 ± 0.0008	0.85
NGC 5474	2.66 ± 0.05	-1.09 ± 0.03	0.592 ± 0.005	-0.228 ± 0.004	1.056 ± 0.004	0.58
NGC 5713	3.1 ± 0.3	-1.719 ± 0.010	0.184 ± 0.009	-0.73 ± 0.02	1.240 ± 0.013	0.87
NGC 5866	1.8 ± 0.2	-1.89 ± 0.02	0.329 ± 0.005	-0.483 ± 0.007	0.21 ± 0.04	0.83
NGC 6822	0.969 ± 0.008	-0.951 ± 0.010	0.5762 ± 0.0016	-0.2394 ± 0.0012	0.9146 ± 0.0018	0.73
NGC 6946	5.80 ± 0.13	-2.02 ± 0.11	0.380 ± 0.002	-0.420 ± 0.002	0.562 ± 0.014	0.78
NGC 7331	2.22 ± 0.07	-1.469 ± 0.010	0.397 ± 0.002	-0.401 ± 0.003	0.448 ± 0.005	0.80
NGC 7552	3.1 ± 0.4	-2.47 ± 0.04	0.093 ± 0.007	-1.03 ± 0.03	0.27 ± 0.02	0.91
NGC 7793	2.20 ± 0.04	-1.054 ± 0.017	0.469 ± 0.003	-0.329 ± 0.002	0.5105 ± 0.0005	0.65

[a] These data have been corrected for inclination effects using Equation 9.
[b] These data have been corrected for inclination effects using Equation 10.
[c] These data have been corrected for distance-related effects using Equation 8.

Table 11. Statistics on 3.6 μm Morphological Parameters for Different Hubble Types

Hubble Type	Number of Galaxies	C^a	$\overline{M}_{20}{}^a$	$\log(\overline{R}_{eff})^a$	A^a	G^a
All	71	3.00 ± 0.09	-2.03 ± 0.08	-0.47 ± 0.02	0.18 ± 0.03	0.637 ± 0.017
E-S0	11	3.1 ± 0.2	-2.20 ± 0.07	-0.49 ± 0.06	0.09 ± 0.03	0.65 ± 0.02
S0/a-Sab	15	3.50 ± 0.17	-2.37 ± 0.07	-0.50 ± 0.04	0.12 ± 0.02	0.70 ± 0.02
Sb-Sbc	13	3.37 ± 0.17	-2.41 ± 0.09	-0.49 ± 0.02	0.16 ± 0.03	0.682 ± 0.015
Sc-Sd	19	2.71 ± 0.13	-1.73 ± 0.09	-0.36 ± 0.04	0.27 ± 0.04	0.630 ± 0.019
Sdm-Im	13	2.44 ± 0.11	-0.88 ± 0.14	-0.46 ± 0.05	0.69 ± 0.08	0.48 ± 0.03

[a] These are median values and standard deviations of the means.

Table 12. Statistics on 24 μm Morphological Parameters for Different Hubble Types

Hubble Type	Number of Galaxies	C^a	$\overline{M}_{20}{}^a$	$\log(\overline{R}_{eff})^a$	A^a	G^a
All	73	2.51 ± 0.14	-1.47 ± 0.08	-0.50 ± 0.03	0.59 ± 0.06	0.764 ± 0.012
E-S0	11	2.6 ± 0.3	-2.23 ± 0.17	-0.80 ± 0.06	0.25 ± 0.09	0.83 ± 0.03
S0/a-Sab	16	3.0 ± 0.3	-2.07 ± 0.18	-0.60 ± 0.06	0.35 ± 0.07	0.77 ± 0.03
Sb-Sbc	13	3.0 ± 0.3	-1.47 ± 0.18	-0.50 ± 0.08	0.45 ± 0.08	0.82 ± 0.02
Sc-Sd	19	2.3 ± 0.3	-1.14 ± 0.10	-0.41 ± 0.04	0.69 ± 0.05	0.745 ± 0.019
Sdm-Im	14	2.0 ± 0.3	-1.01 ± 0.15	-0.48 ± 0.05	1.24 ± 0.20	0.68 ± 0.03

[a] These are median values and standard deviations of the means.

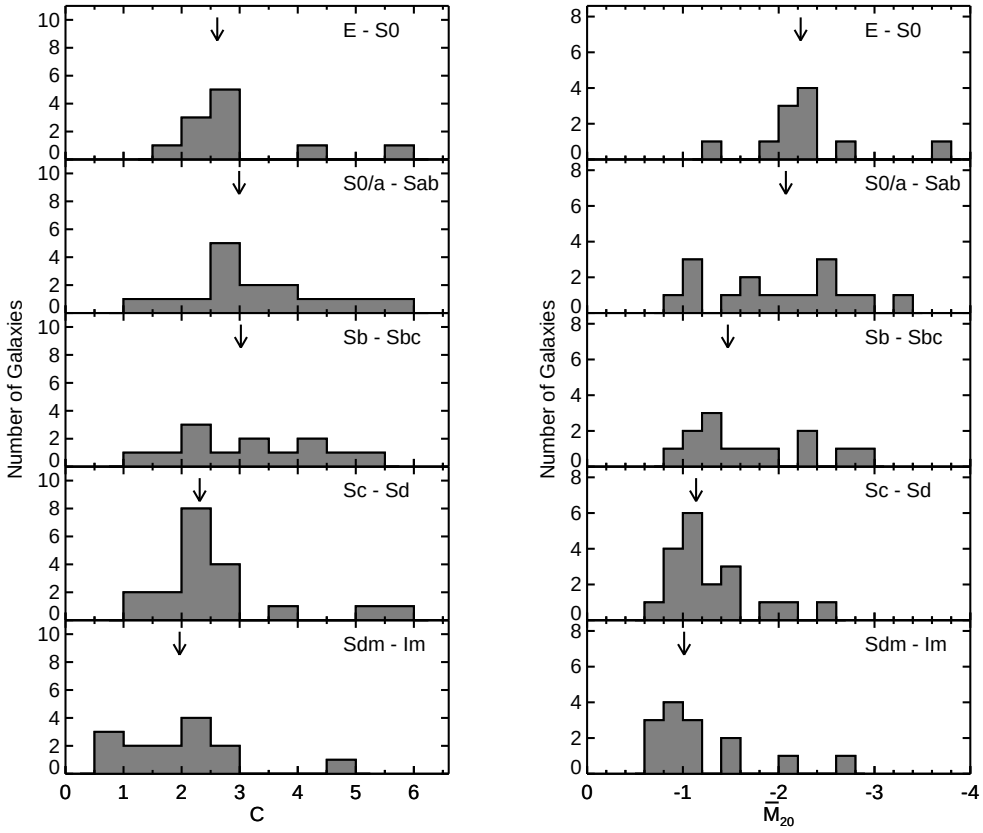

Figure 4. Histograms of the 24 μm C and $\overline{M}_{20}$ parameters sorted according to Hubble type. The parameters are plotted so that more concentrated (higher C, lower $\overline{M}_{20}$) values appear on the right. The arrow indicates the median value for each subgroup (with the average of the two central values used to calculate the median in subgroups with an even number of members). See Section 4.1 for discussion.

for better comparisons between this paper's results and the results of Conselice (2003).

4 TRENDS IN THE MORPHOLOGICAL PARAMETERS WITH HUBBLE TYPE

4.1 Statistical Analysis of the Trends in the Morphological Parameters

Table 9 gives the morphological parameters measured from the 3.6 μm data, and Table 10 gives the parameters measured from the 24 μm data. Medians and standard deviations of the means for the parameters as a function of Hubble type are given in Tables 11 and 12. To examine the variations versus morphology, similar Hubble types have been grouped together (i.e. S0/a-Sab; Sb-Sbc, etc.). As an additional test of the trends in the morphological parameters, we have applied the Kolmogorov-Smirnov (K-S) test, which gives the probability that individual parameters for the S0/a-Sab and Sc-Sd galaxies are drawn from the same distribution. If this probability is lower than 1%, the S0/a-Sab values are statistically different from the Sc-Sd values. (A 1% probability that two populations are drawn from the same distribution should be equivalent to a 3σ difference between the median values of the two populations.) The results of this test on the 24 μm morphological parameters is given in Table 13.

Although both the 3.6 and 24 μm morphological parameters are presented here, the emphasis of the analysis in this section is placed on the 24 μm morphological parameters, since variations in stellar morphologies along the Hubble sequence are already well-understood. We note that the 3.6 μm morphological parameters show that starlight is more centrally concentrated and more symmetric in early-type galaxies and more extended and asymmetric in late-type galaxies, as is expected from the definition of the Hubble sequence (Hubble 1926). Moreover, the parameters derived here match the R-band morphological parameters derived for normal spiral galaxies by Conselice (2003) and Lotz et al. (2004). However, we save the detailed discussion about the 3.6 μm parameters for Section 6.1, where the stellar morphological parameters are compared to the 24 μm morphological parameters. The rest of this section is used to search for possible trends in the 24 μm morphological parameters along the Hubble sequence.

Figure 4 shows how the 24 μm C and $\overline{M}_{20}$ parameters vary with morphological type. The C parameter only appears to vary slightly between S0/a-Sab and Sc-Sd galaxies, but it is significantly lower in Sdm-Im galaxies. The weak variations in the C parameter may partly reflect its ineffectiveness as a measure of central concentration. Stronger trends are visible in the $\overline{M}_{20}$ parameter as a function of Hubble type, where a strong difference can be seen between S0/a-Sab and Sc-Sd galaxies. These trends are also reflected

Table 13. Results on Applying K-S Test to 24 μm Morphological Parameters for S0/a-Sab and Sc-Sd Galaxies

Parameter	Probability[1]
C	0.025
$\overline{M}_{20}$	0.0023
$\log(\overline{R}_{eff})$	0.099
A	0.013
G	0.27

[a] This is the probability that the tested parameter for the S0/a-Sab and Sc-Sd data have the same distribution. A probability of ~ 0.01 is interpreted as having the same significance as a 3σ difference between the median values for the S0/a-Sab and Sc-Sd galaxies.

in both the statistics in Table 12 and the results from the K-S test in Table 13. The results demonstrate that the central concentration of 24 μm emission varies across the Hubble sequence, with the emission being the most centrally concentrated in E-S0 galaxies and the most diffuse in Sdm-Im galaxies. Note the statistically significant variations between S0/a-Sab and Sc-Sd galaxies.

Figure 5 shows how the 24 μm $\log(\overline{R}_{eff})$ parameter varies with morphological type. Along with the statistical information in Tables 12 and 13, Figure 5 shows general trends in $\log(\overline{R}_{eff})$ as a function of Hubble type, with the most centralized infrared emission found in E-S0 galaxies and the most extended emission found in Sdm-Im galaxies. However, the statistical significance of the difference between the distribution of $\log(\overline{R}_{eff})$ for S0/a-Sab and Sc-Sd galaxies is relatively weak. The difference between the values in Table 12 is less than 3σ, and the K-S test indicates that the probability that the S0/a-Sab and Sc-Sd data come from the same distribution is $\sim 10\%$ (whereas a 1% probability would be the equivalent of a 3σ difference). Despite the weak statistical significance of the difference between S0/a-Sab and Sc-Sd galaxies, these results still indicate that the 24 μm emission is relatively centralized in early-type spiral galaxies but relatively extended in late-type spiral galaxies.

Figure 6 shows how the 24 μm A parameter varies with morphological type. A trend with morphological type is seen with this parameter as well, with E-S0 galaxies showing the most symmetric emission and Sdm-Im galaxies showing the most asymmetric emission. Again, the results in Tables 12 and 13 show that statistically significant differences can be seen between the S0/a-Sab and Sc-Sd galaxies, although the variations are close to the 3σ level. Also note the relatively large dispersion in values for Sdm-Im galaxies.

Figure 7 shows how the 24 μm G parameter varies with morphological type. The variations in this parameter are weak. Statistically, no significant change is observed between E and Sd galaxies, although some Sc-Sd galaxies have G values that are lower than the G parameters for most E-Sbc galaxies. This may indicate that the same fraction of 24 μm emission originates from bright peaks in most early- and late-type spiral galaxies, regardless of how the bright peaks are distributed within the galaxies, and that only a few late-type spiral galaxies contain relatively more high surface brightness 24 μm emission from diffuse or extended sources. Sdm-Im galaxies typically have slightly lower G values than other galaxies, indicating that the infrared emission is more evenly distributed than other galaxy types. However strong variations in G among the Sdm-Im galaxies are visible, which indicates that some Sdm-Im galaxies have very evenly-distributed emission while others have point-like emission.

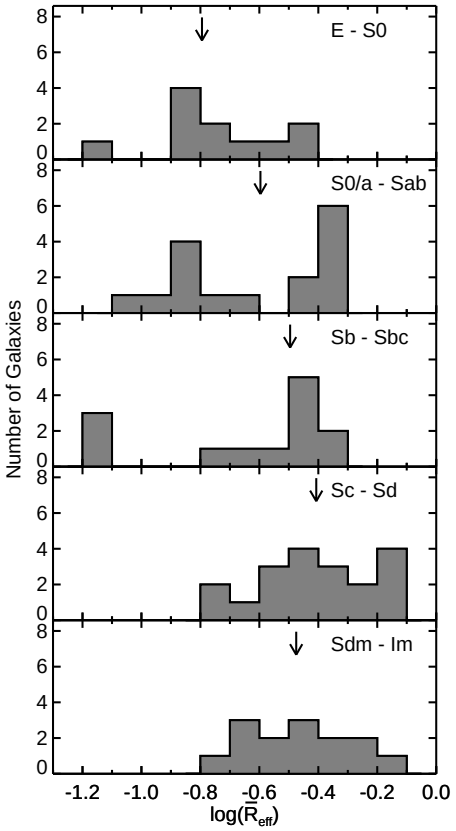

Figure 5. Histograms of the 24 μm $\log(\overline{R}_{eff})$ parameter sorted according to Hubble type. Higher $\log(\overline{R}_{eff})$ values correspond to dust emission that is more extended relative to the optical disc. The arrow indicates the median value for each subgroup (with the average of the two central values used to calculate the median in subgroups with an even number of members, which is why the median does not appear to correspond to any galaxy in one of the panels). See Section 4.1 for discussion.

Overall, these results reveal a clear trend in the distribution of 24 μm dust emission along the Hubble sequence. 24 μm emission is generally compact (relative to itself and relative to stellar emission) and symmetric in E-S0 galaxies. In S0/a-Sab galaxies, the dust emission is only slightly more extended; the discs are generally only a weak source of emission. In Sc-Sd galaxies, nuclear dust emission is still present, but a much greater fraction of the emission originates from the discs of the galaxies, as reflected by the high $\overline{M}_{20}$ and $\log(\overline{R}_{eff})$ values. The dust emission in the discs also appears to be more asymmetric. Finally, in Sdm-Im galaxies, the galaxies' structure is disorganized, resulting in highly extended, highly asymmetric dust emission.

Some of the Sdm-Im galaxies are exceptions to the trends seen with the other galaxies in this sample. The 24 μm $\overline{M}_{20}$, $\log(\overline{R}_{eff})$, A, and G parameters for these galaxies span a broad range of values. Some objects, such as DDO 53 and

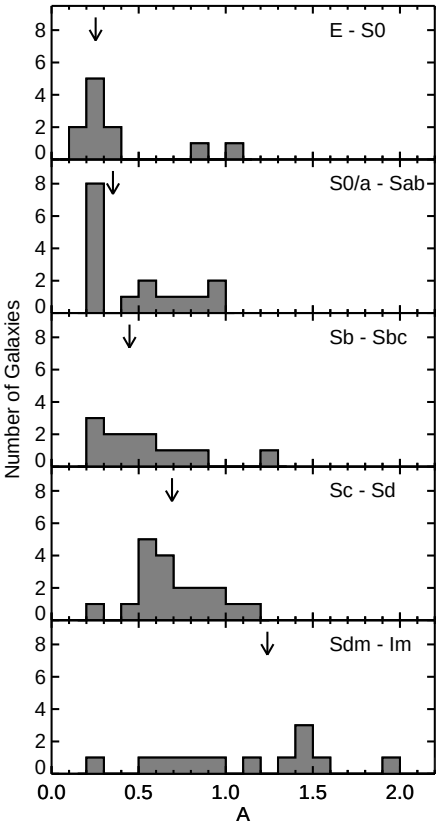

Figure 6. Histograms of the 24 μm A parameter sorted according to Hubble type. Higher A values correspond to higher asymmetry. Note that the Im galaxy Ho I, with $A = 3.28 \pm 0.11$, falls to the right of the plot range in the bottom histogram. The arrow indicates the median value for each subgroup (with the average of the two central values used to calculate the median in subgroups with an even number of members, which is why the median does not appear to correspond to any galaxy in two of the panels). See Section 4.1 for discussion.

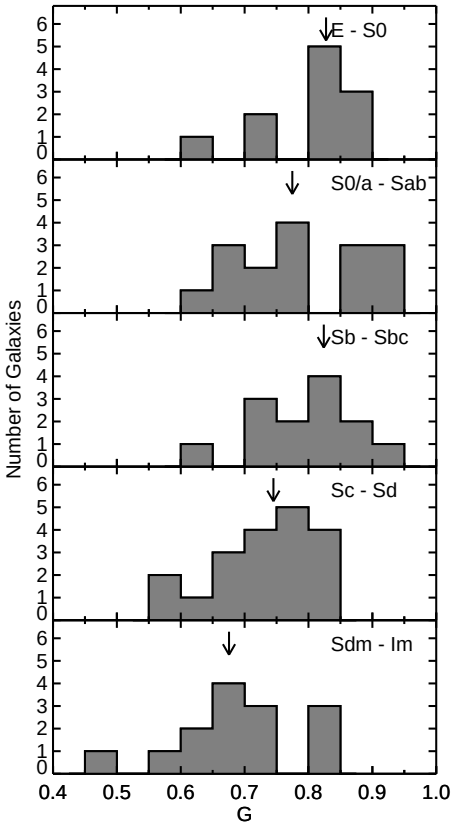

Figure 7. Histograms of the 24 μm G parameter sorted according to Hubble type. Higher G values correspond to flux being concentrated in a few bright knots; lower G values correspond to dust emission being more evenly distributed. The arrow indicates the median value for each subgroup (with the average of the two central values used to calculate the median in subgroups with an even number of members). See Section 4.1 for discussion.

Mrk 33, are compact sources, while other galaxies, such as NGC 5408 and Ho II, are highly extended, asymmetric objects. Also worth noting are the Im galaxies not included in this analysis because they were effectively non-detections in one or more MIPS bands, including DDO 154, DDO 165, Ho IX, M81 Dwarf A, and M81 Dwarf B. This is discussed further in Section 6.4.

4.2 Galaxies with Representative 24 μm Morphologies

Based on the 24 μm parameters, we can compare galaxies of a given Hubble type and determine which galaxies are representative of each type in the 24 μm wave band. We show the 24 μm images of these representative galaxies in Figure 8. The galaxies in Figure 8 were selected on the basis that their morphological parameters are statistically equivalent to the median morphological parameters for the given Hubble type. They sometimes contrast with nearby or well-studied galaxies where the structure of the 24 μm dust emission (and possibly the structure of the ISM) can be very peculiar for its particular Hubble type.

The galaxies in Figure 8 qualitatively illustrate the variations in the distribution of 24 μm emission that were found quantitatively in Section 4.1. The 24 μm emission from elliptical and S0 galaxies (when present) is generally from a central, point-like or compact source. In S0/a-Sab galaxies, the nucleus is still the predominant source of emission, and the dust outside the nucleus is generally axisymmetric. Often, some of the dust is located in ring-like structures as seen in NGC 3185 and NGC 4736. The 24 μm emission is relatively compact compared to the optical disc of the galaxy. Progressing through Sb-Sbc to Sc-Sd galaxies, 24 μm emission from the disc becomes relatively strong compared to the nucleus. In many Sc-Sd galaxies, the nucleus is often no longer the brightest source of emission, and the dust emission appears only loosely organized. Finally, in Sdm-Im galaxies, the 24 μm emission appears amorphous, although, as noted in the previous section, the distribution of 24 μm emission in Sdm-Im galaxies is quite varied.

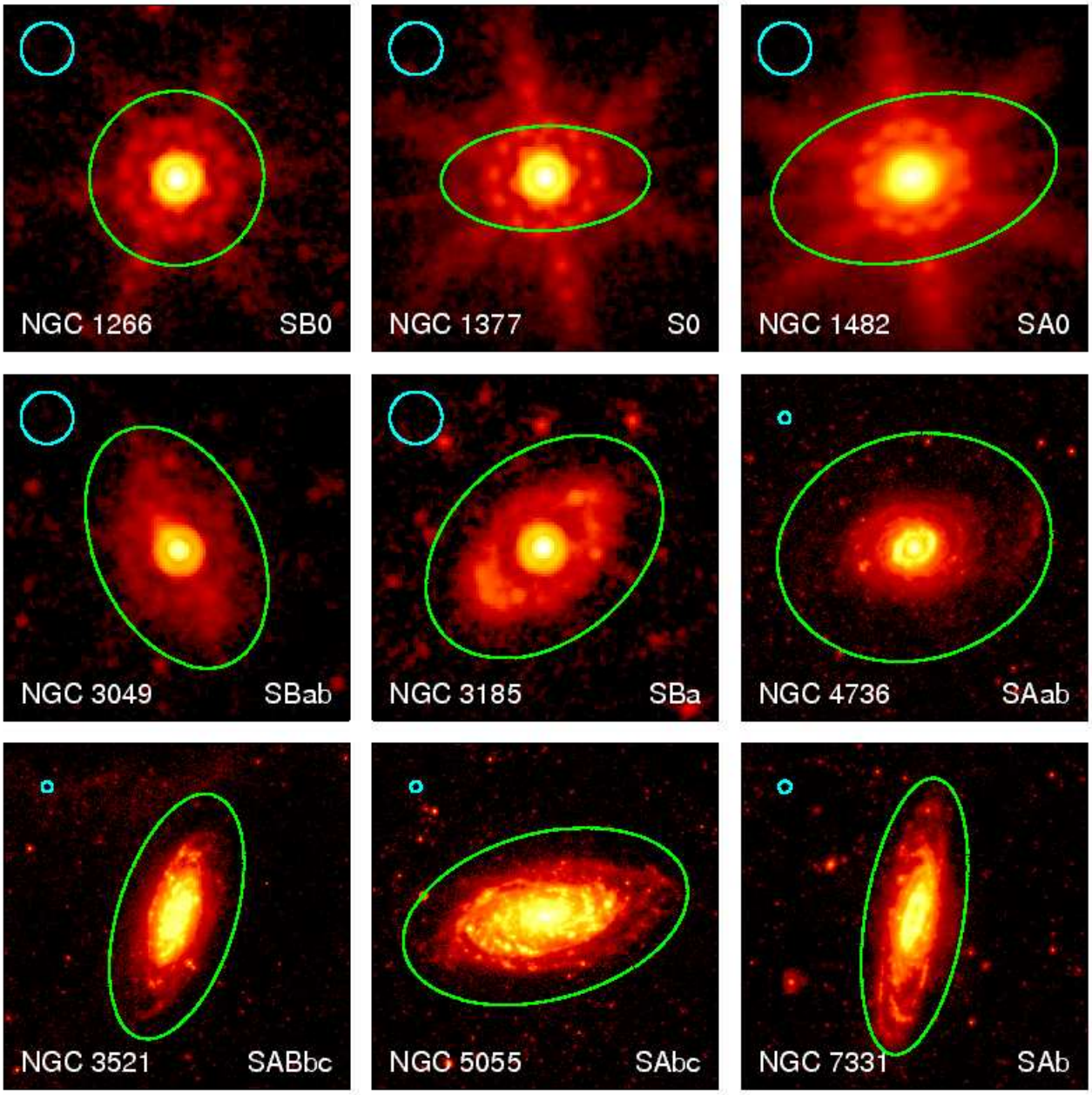

Figure 8. 24 μm images of galaxies with typical morphological parameters for their Hubble types (see Section 4.2). Each row contains galaxies with similar Hubble types. The images are ordered from E-S0 in the top row to Sdm-Im in the bottom row. The Hubble type of each galaxy (from RC3) is listed in the lower corner of each image. The D_{25} isophote from RC3 is overplotted on the data. An 18 arcsec circle representing three times the FWHM of the 24 μm data is plotted in the upper left corner of the images. Note that most of the extended structure in the NGC 1266, NGC 1377, and NGC 1482 images are mostly the PSF of the unresolved or marginally resolved central sources, and some of the extended structure in the NGC 3049 image is also related to the PSF of the central source.

4.3 Galaxies with Peculiar 24 μm Morphologies

The outliers from the trends in the 24 μm parameters with Hubble type are also worth noting simply because they show how AGN activity, starburst activity, or dynamical processes can affect either dust heating or the distribution of dust within the galaxies. Four examples of notable peculiar sources (where the 24 μm morphological parameters differ from the median values by a large number of standard deviations) are listed below, with their 24 μm images shown in alphanumeric order in Figure 9.

NGC 1316 (Fornax A). Compared to other E-S0 galaxies, the 24 μm emission is unusually centrally concentrated and unusually asymmetric. This is exceptional because the 24 μm emission in E-S0 galaxies is already centrally concentrated compared to other Hubble types. This galaxy is a radio galaxy (Wade 1961) that has undergone multiple interactions (Schweizer 1980). The central far-infrared emission from this galaxy is probably strongly enhanced by the AGN activity. Moreover, the interactions have triggered gas infall into the nucleus (Schweizer 1980), which would also

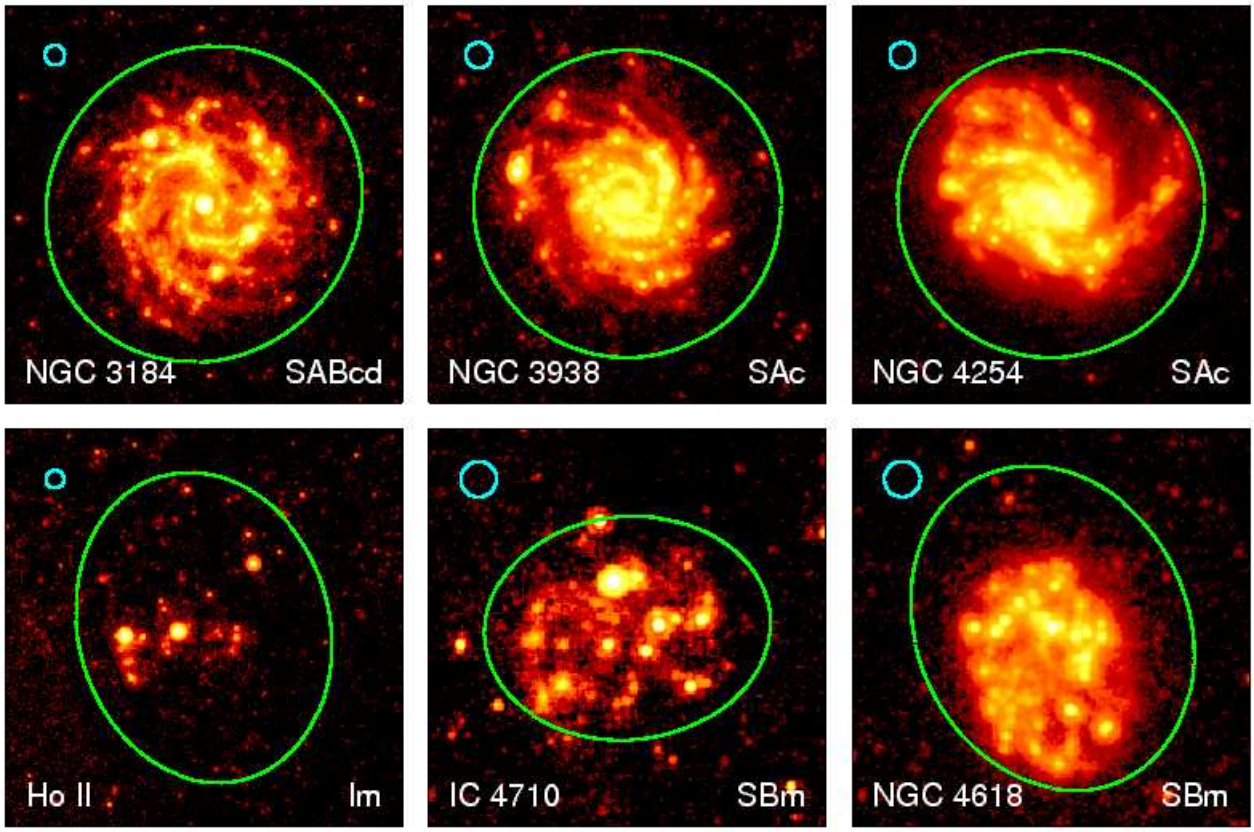

Figure 8 – *continued*

make the 24 μm appear centrally concentrated. These interactions may also explain the asymmetric appearance of the galaxy at 24 μm. Note that AGN may also be responsible for producing centrally concentrated 24 μm emission in some of the other E-S0 galaxies as well.

NGC 4536. The 24 μm emission is unusually centrally concentrated in NGC 4536 compared to other Sb-Sbc galaxies as demonstrated by the low $\overline{M}_{20}$ and $\overline{R}_{eff}$ values. This galaxy is an example of a late-type spiral galaxy with strong nuclear starburst activity (e.g. Puxley et al. 1988; Telesco et al. 1993), which is why the infrared emission appears very centrally concentrated. Other galaxies that contain strong nuclear star formation activity, including NGC 4631 (e.g. Rand et al. 1992) and NGC 6946 (e.g. Turner & Ho 1983; Devereux & Young 1993; Telesco et al. 1993), also appear unusually centrally concentrated at 24 μm.

NGC 4725. A significant amount of the 24 μm emission from NGC 4725 is associated with the galaxy's asymmetric outer ring (e.g. Buta 1988). Consequently, the 24 μm emission from the galaxy is the most extended and asymmetric of all the S0/a-Sab galaxy in the sample. NGC 1291 also contains a dusty outer ring structure that also makes it appear unusually extended at 24 μm, although it does not appear as extended or asymmetric as NGC 4725.

NGC 5033. This galaxy has a Seyfert 1.5 nucleus (Ho et al. 1997b). As a consequence, the 24 μm emission appears to be enhanced by the AGN activity, so the 24 μm emission is more centrally concentrated than the average Sc-Sd galaxy. Note that some of the other Seyfert galaxies in this sample, such as NGC 3185 (Ho et al. 1997b), are also very compact.

5 VARIATIONS IN 24 μM PARAMETERS BETWEEN BARRED AND UNBARRED SPIRAL GALAXIES

The effects of bars on the ISM of galaxies has been well documented. Both observations (e.g. Sakamoto et al. 1999; Sheth et al. 2005) and theoretical models (e.g. Athanassoula 1992; Friedli & Benz 1993) have demonstrated that bars drive gas into the centres of spiral galaxies. Consequently, bars may enhance nuclear star formation activity (e.g. Huang et al. 1996; Ho et al. 1997a; Roussel et al. 2001), although some observational studies have demonstrated that not all galaxies with bars have enhanced nuclear star formation (e.g. Martinet & Friedli 1997; Bendo & Joseph 2004). Nonetheless, if bars do enhance nuclear star formation, then the 24 μm morphological parameters should demonstrate that the 24 μm emission in barred galaxies is more compact and possibly more peaked compared to unbarred galaxies.

To examine the effects of bars, we compared the 24 μm morphological parameters of unbarred (SA), weakly barred (SAB), and strongly barred (SB) galaxies. Comparison are made for all spiral (S0/a-Sd) galaxies and for subsets of spiral galaxies divided according to their Hubble type. Table 14 shows the median and standard deviations of the C, $\overline{M}_{20}$, $\overline{R}_{eff}$, and G parameters of SA, SAB, and SB galaxies, and

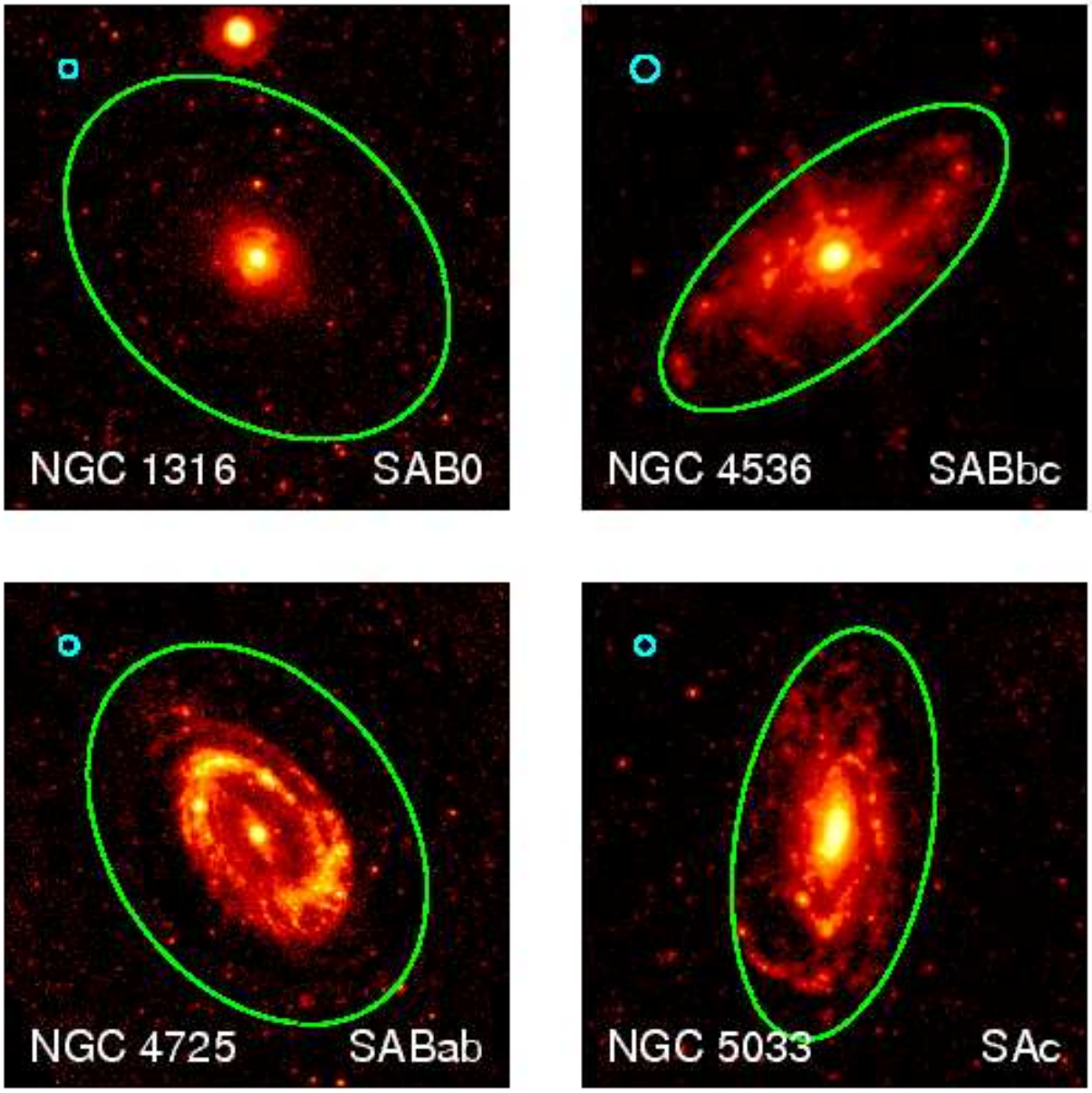

Figure 9. 24 μm images of galaxies with peculiar morphological parameters for their Hubble types (see Section 4.3). The images are ordered alphanumerically. See Figure 8 for information on the overplotted lines and the Hubble type. In the image of NGC 4536, the spike-like features perpendicular to the major axis of the galaxy and the central ring structure is part of PSF of the marginally-resolved central starburst.

Table 15 shows the results from the K-S test when applied to subsets of SA and SB galaxies. Additionally, Figure 10 shows histograms of the C, $\overline{M}_{20}$, and $\overline{R}_{eff}$ parameters for S0/a-Sd galaxies separated according to their bar type.

These results generally demonstrate a difference between SA and SB galaxies, with SB galaxies having more centrally concentrated 24 μm emission as seen in higher C, lower $\overline{M}_{20}$, and lower $\overline{R}_{eff}$ parameters and more emission located in peaks as seen in the higher G parameter. However, the trends are only significant at the 3σ level when all spiral galaxies (all S0/a-Sd galaxies) are used in the analysis. Since the SA galaxies for this sample tend to be a slightly later type than the SB galaxies for this sample, the results from comparing all unbarred spiral galaxies to all barred spiral galaxies may be partly biased by trends along the Hubble sequence (although G should exhibit this bias). When subsets of spiral galaxies (only S0/a-Sab, only Sb-Sbc, or only Sc-Sd galaxies) are examined, SA galaxies may still be differentiated from SB galaxies, but the results are not as statistically significant. Unfortunately, when the galaxies in this sample are divided according to both Hubble type and bar type, the resulting subsets are relatively small; all subsets contain fewer than 10 galaxies, and some subsets contain fewer than 5 galaxies. We conclude that bars may

Table 14. Statistics on 24 μm Morphological Parameters for Different Bar Types

Hubble Type	Bar Type	Number of Galaxies	C^a	$\overline{M}_{20}{}^a$	$\log(\overline{R}_{eff})^a$	G^a
S0/a-Sd	SA	21	2.66 ± 0.16	-1.24 ± 0.11	-0.39 ± 0.05	0.72 ± 0.02
	SAB	15	2.5 ± 0.4	-1.25 ± 0.19	-0.53 ± 0.06	0.80 ± 0.02
	SB	12	4.1 ± 0.4	-2.31 ± 0.17	-0.70 ± 0.09	0.81 ± 0.02
S0/a-Sab	SA	7	2.8 ± 0.2	-1.7 ± 0.2	-0.39 ± 0.10	0.72 ± 0.04
	SAB	3	2.4 ± 1.2	-1.7 ± 0.7	-0.70 ± 0.15	0.80 ± 0.06
	SB	6	4.5 ± 0.5	-2.47 ± 0.19	-0.70 ± 0.11	0.85 ± 0.05
Sb-Sbc	SA	4	2.8 ± 0.3	-1.24 ± 0.10	-0.35 ± 0.03	0.78 ± 0.04
	SAB	7	3.1 ± 0.5	-1.7 ± 0.3	-0.56 ± 0.09	0.83 ± 0.02
	SB	2	5.2 ± 0.6	-2.34 ± 0.16	-1.1282 ± 0.019	0.89 ± 0.03
Sc-Sd	SA	10	2.2 ± 0.2	-1.09 ± 0.16	-0.33 ± 0.06	0.72 ± 0.03
	SAB	5	2.5 ± 0.7	-1.1 ± 0.2	-0.42 ± 0.06	0.77 ± 0.03
	SB	4	2.8 ± 0.7	-1.41 ± 0.14	-0.37 ± 0.13	0.797 ± 0.017

[a] These are median values and standard deviations of the means.

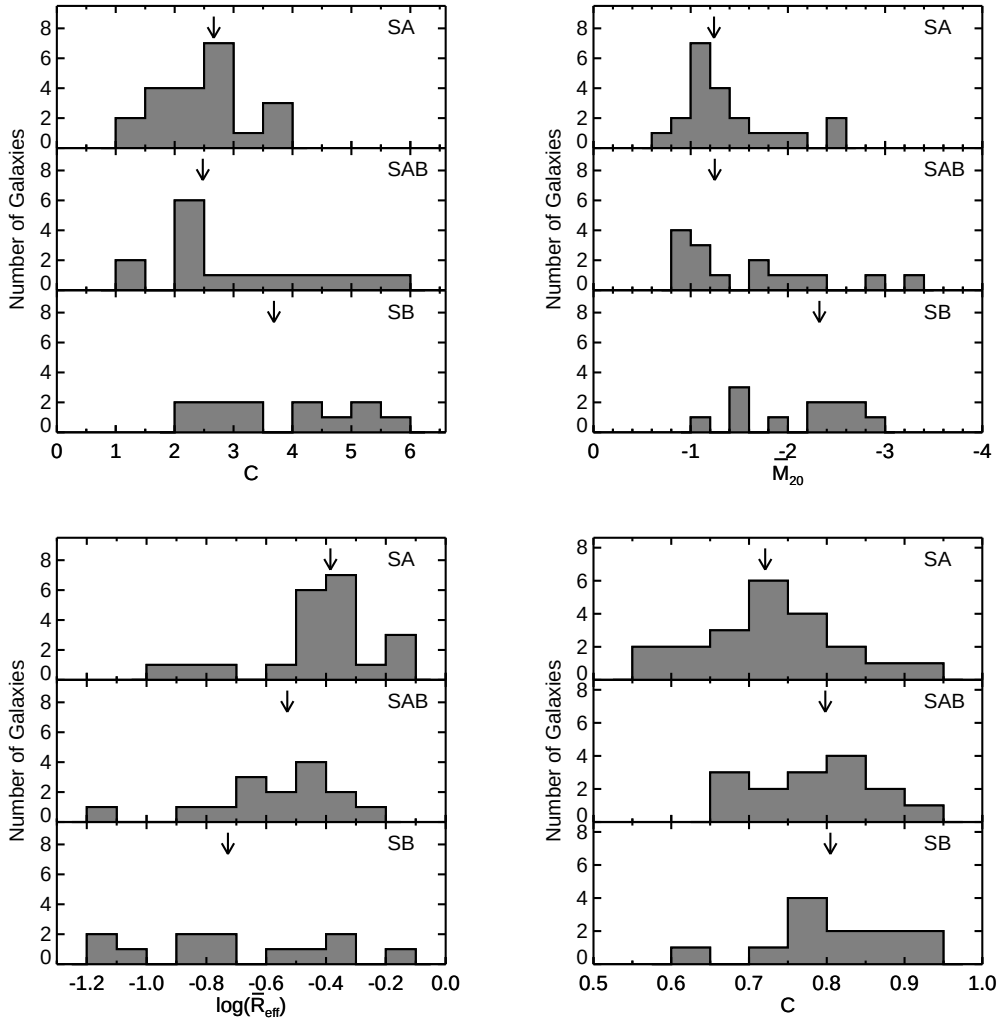

Figure 10. Histograms of the 24 μm C, $\overline{M}_{20}$, and $\log(\overline{R}_{eff})$ parameters for all S0/a-Sd galaxies sorted according to bar type. The C and lower $\overline{M}_{20}$ parameters are plotted so that more concentrated (higher C, lower $\overline{M}_{20}$) values appear on the right. The $\log(\overline{R}_{eff})$ parameter is plotted so that more extended (larger $\log(\overline{R}_{eff})$ values fall on the right. The arrow indicates the median value for each subgroup (with the average of the two central values used to calculate the median in subgroups with an even number of members, which is why the median does not appear to correspond to any galaxy in one of the panels). See Section 5 for discussion.

Table 15. Results on Applying K-S Test to 24 μm Morphological Parameters for SA and SB Galaxies

Hubble Type	Parameter	Probability[a]
S0/a-Sd	C	0.018
	$\overline{M}_{20}$	0.0060
	$\log(\overline{R}_{eff})$	0.0095
	G	0.015
S0/a-Sab	C	0.19
	$\overline{M}_{20}$	0.048
	$\log(\overline{R}_{eff})$	0.19
	G	0.54
Sb-Sbc	C	[b]
	$\overline{M}_{20}$	[b]
	$\log(\overline{R}_{eff})$	[b]
	G	[b]
Sc-Sd	C	0.16
	$\overline{M}_{20}$	0.24
	$\log(\overline{R}_{eff})$	0.90
	G	0.064

[a] This is the probability that the tested parameter for the SA and SB data have the same distribution. A probability of ~ 0.01 is interpreted as having the same significance as a 3σ difference between the median values for the S0/a-Sab and Sc-Sd galaxies.
[b] The K-S test results are not meaningful unless each dataset contains at least four values. The K-S test would compare a set of 4 values to a set of 2 values in this particular case, so these probabilities would have no meaningful interpretation and are not reported here.

play a role in changing the 24 μm morphologies of nearby galaxies, which would be consistent with previous observations of barred spiral galaxies, but that a larger sample of spiral galaxies is needed to examine these trends in more detail.

Although the analysis is not entirely conclusive in detecting differences between barred and unbarred galaxies, we note that the results do show differences between barred and unbarred galaxies in both the early-type spiral galaxy subset and the late-type spiral galaxy subset. Most recent observations show that bars only enhance nuclear star formation activity in early-type spiral galaxies (Ho et al. 1997a; Roussel et al. 2001), which implies that bars should only affect the 24 μm morphologies of early-type spiral galaxies. However, we should emphasize that comparing the 24 μm morphological parameters to measurements of nuclear star formation activity may not be appropriate. Although the 24 μm morphologies show that the distribution of star formation itself changes, it cannot be used to show changes in the relative strength of star formation activity (i.e. the ratio of current to past star formation activity, or the star formation activity per unit total stellar mass). A comparison of the morphological parameters to measurements of the relative star formation activity is needed to better understand the trends shown by the morphological parameters.

6 DISCUSSION

6.1 Comparison to Results on Stellar Morphologies

We compared the 24 μm morphological parameters for the data in Table 10 to the data for 3.6 μm morphological parameters in Table 9 and to the R-band morphological parameters given in Conselice (2003). In general, the 24 μm parameters differ significantly from the 3.6 μm and R-band parameters. For an individual Hubble type, the 24 μm emission appears more extended then the 3.6 μm or R-band emission, as seen by the lower C, higher $\overline{M}_{20}$, and higher $\log(\overline{R}_{eff})$ parameters. The 24 μm emission also appears more asymmetric, as indicated by the higher A parameters, and more of the 24 μm emission appears to originate in one or a few bright peaks, as exhibited by the higher G parameter. (Note, however, that the 3.6 μm C and A parameters in Table 9 are comparable to the same R-band parameters given by Conselice (2003).)

In Figure 11, we show comparisons of the morphological parameters to each other that may be directly compared with Figure 15 in Conselice (2003) and Figures 10-14 in Lotz et al. (2004). The parameter space occupied by the 3.6 μm SINGS data is similar to the parameter space occupied by the R-band data in Conselice and Lotz et al. This is expected, as both the 3.6 μm wave band and the R-band trace the starlight from all stars within the host galaxies, including evolved red stars. However, the parameter space occupied by the 24 μm morphological parameters for the SINGS galaxies do not correspond to the same parameter space occupied by the 3.6 μm morphology data for the SINGS galaxies or the R-band morphology data for normal galaxies in Conselice (2003) and Lotz et al. (2004). The offset between the 3.6 and 24 μm parameters is most easily seen in the plots of $\overline{M}_{20}$ versus G, C versus G, and A versus G. However, note that the 24 μm C and A parameters for the SINGS galaxies are comparable to the corresponding R-band parameters for starbursts and mergers in Conselice (2003), and the 24 μm data occupy a similar location in parameter space as the R-band data for ULIRGs in Lotz et al. (2004).

Aside from showing the differences between the distribution of starlight and 24 μm emission in nearby galaxies, these results demonstrate that individual wave bands need to be calibrated at rest wavelengths to determine the parameter spaces occupied by both normal and merging galaxies. It may also be desirable to demonstrate that morphological parameters measured in wave bands that are sensitive to star formation can still be used to separate mergers and starbursts from normal galaxies, especially given that the 24 μm morphological parameters for the galaxies in this paper statistically match the R-band morphological parameters for starbursts and ULIRGs.

Despite the differences in the parameter values between the 24 μm wave band and stellar wave bands, the 24 μm morphological parameters show variations along the Hubble sequence that are similar to those seen in the 3.6 μm morphological parameters as well as the R-band parameters from Conselice (2003). The morphological parameters measured in stellar wave bands and at 24 μm show that elliptical and early-type spiral galaxies are generally compact and symmetric whereas late-type spiral galaxies are more

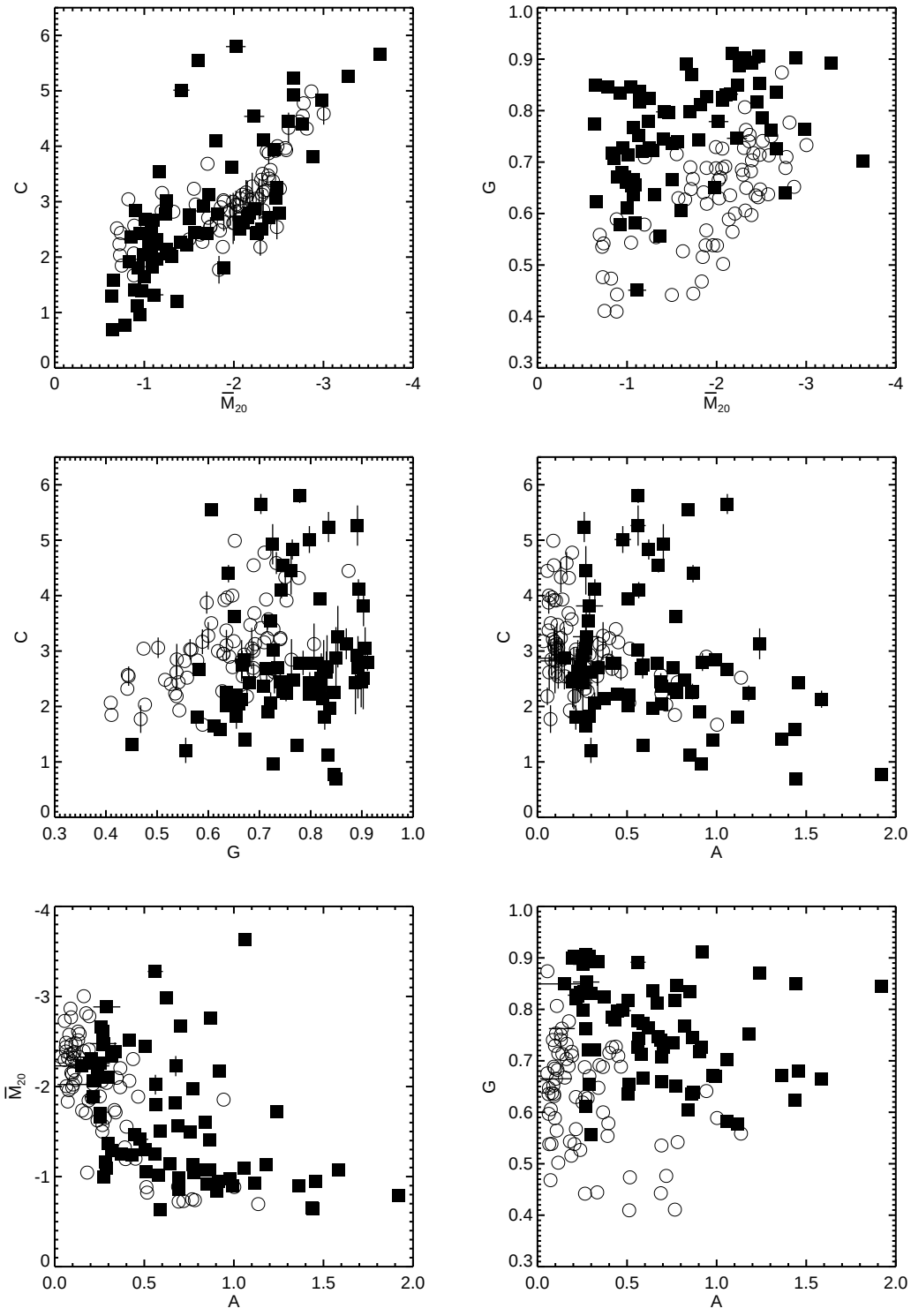

Figure 11. Plots of the 3.6 μm (open circles) and 24 μm (filled squares) morphological parameters versus each other. These plots are meant to be directly compared with Figures 10-14 in Lotz et al. (2004) although the scales of the x- and y-axes are slightly different. The plot of C versus A may also be compared to Figure 15 of Conselice (2003), although Conselice plots the data differently. Note that Ho I, which has a 24 μm asymmetry of 3.28 ± 0.11, falls outside some of the plots. See Section 6.1 for discussion.

extended and asymmetric. Moreover, the differences in the 24 μm asymmetry between early- and late-type spiral galaxies observed here does resemble the trends in lopsidedness observed in near-infrared observations of nearby galaxies by Bournaud et al. (2005). The G parameter is the only parameter where the trends seen at 24 μm differ from those seen in stellar wave bands. Slightly more 3.6 μm emission appears to originate from one or a few bright peaks in early-type spiral galaxies when compared to late-type spiral galaxies, but the same fraction of 24 μm emission is located in bright peaks in both early- and late-type spiral galaxies. Nonetheless, we conclude that the variations in stellar morphologies along the Hubble sequence are interrelated with the dust morphologies and implicitly with the morphologies of the ISM and the distribution of star formation regions.

6.2 Comparison to Results on the Distribution of the ISM and Star Formation

The observed trends in the central concentration and spatial extent of the 24 μm dust emission along the Hubble sequence are similar to those observed at 12 and 60 μm by Bendo et al. (2002), at 850 μm by Thomas et al. (2004), and at 8 μm by Pahre et al. (2004). However, the results from the analysis in this paper illustrate the trend more robustly than these previous studies; the analysis in this paper is quantitative instead of qualitative, the images used in this paper completely cover the optical discs of all the galaxies, and the sample in this paper contains several galaxies of each Hubble type. Interestingly, the same variations in the spatial distribution of dust emission are found regardless of the wave band used. This implies that a single wave band can be used to roughly characterize the spatial extent of all the dust emission on global scales, although colour variations within galaxies, such as those observed by Dale et al. (2005), Calzetti et al. (2005), Perez-Gonzalez et al. (2006), and Bendo et al. (2006), indicate that a single wave band cannot be used to accurately trace the total dust emission on kpc scales.

The weak relationship between morphology and the effective radius of the 24 μm emission is similar to the trend observed with molecular gas by Young et al. (1995), which demonstrated that molecular gas was found in more central concentrations in early-type galaxies and in wider distributions in Sc galaxies. This shows that, for Sa-Sc spiral galaxies, variations in the distribution of 24 μm emission as a function of morphology are related to the variations in the distribution of molecular gas that fuels star formation. The similarities of the trends is somewhat surprising, as both 24 μm and CO emission are expected to trace gas mass in the ISM, but the 24 μm emission is also expected to be highly sensitive to variations in the illuminating radiation field (Dale et al. 2001b). However, since the 24 μm wave band does trace star formation (Calzetti et al. 2005; Perez-Gonzalez et al. 2006) and since the Schmidt law states that star formation is directly related to gas density (Kennicutt 1998b), the relation between the distribution of CO and 24 μm emission does not seem too extraordinary.

However, Young et al. (1995) found that CO was more centrally concentrated in Sd and later types of galaxies than in Sc galaxies, whereas we find the opposite for dust emission. The reason for the difference between the Young et al. results and our results for Sd and later galaxies could be related to three phenomena that would make the CO emission too weak to detect outside the centres of the galaxies. First, the CO line emission may be low in regions with low metallicities (Taylor et al. 1998, e.g.). Second, the ratio of molecular to atomic gas varies as a function of Hubble type (e.g. Young & Knezek 1989), so less molecular gas and hence less CO emission may be present. Therefore, the CO emission in the late-type galaxies of the Young et al. data may only be detectable in the centres. The dust emission, however, may be related to the total gas content in these very late-type galaxies and may be less sensitive to metallicity effects, so it will appear more spatially extended than the CO emission.

We note that the exponential scale lengths of the HI gas normalized by the optical scale lengths in the sample used by Thomas et al. (2004) did not vary with Hubble type, although their sample for the HI analysis contained 2 S0-Sab galaxies. Nonetheless, these results are contrary to the trends for 24 μm dust emission found here and the trends for CO and dust emission found elsewhere. Additional studies of HI are needed to further understand how its distribution varies as a function of Hubble type and its interrelation with dust emission at different wavelengths.

Finally, we observe that the variations in the spatial extent of 24 μm emission with Hubble type are similar to the variations in the radial distributions of HII regions observed by Hodge & Kennicutt (1983). However, the variations we observed in the spatial extent of the 24 μm emission with Hubble type do not agree with Dale et al. (2001a), who found no such variations in the ratio of the spatial extent of Hα and I-band emission among early- and late-type cluster spiral galaxies. The reason for this discrepancy is unclear. One possibility is that the differences in the spatial distribution of star formation among cluster spiral galaxies are relatively small compared to field spiral galaxies, so the Dale et al. sample, comprised entirely of cluster galaxies, would show no variations in the spatial extent of star formation, whereas the sample here, which contains mostly field galaxies, would show such variations. The numbers of Virgo Cluster galaxies in our sample is too small to accurately assess whether the spatial extent of 24 μm emission in early- and late-type spiral galaxies is also invariant within clusters. The observed variations in the spatial extent of the 24 μm emission also appear to contradict the results from Koopmann et al. (2006), who found no such variations in the Hα/R-band scale lengths among spiral galaxies. Because of problems with stellar continuum subtraction, continuum from AGN, and dust extinction, Koopmann et al. needed to exclude the central regions of the galaxies from their analysis. The Hα radial profiles measured by Koopmann et al. therefore would not have been able to show variations in the Hα surface brightnesses in the centres of galaxies among galaxies of different morphologies. Although the 24 μm data are affected by AGN, they are not as strongly affected by stellar continuum or dust extinction problems, so they may show more accurate variations in the spatial extent of star formation among galaxies of different morphologies.

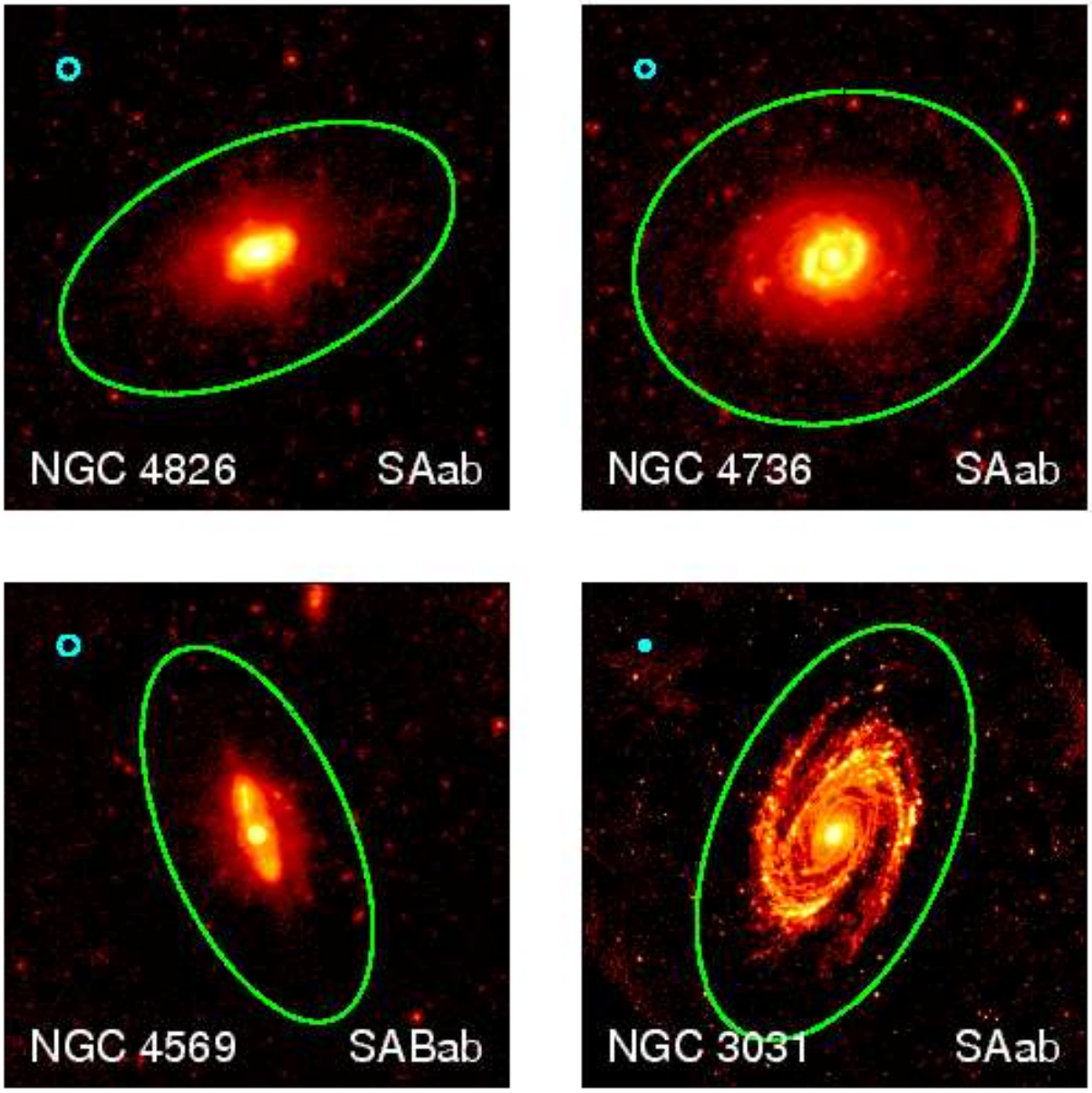

Figure 12. 24 μm images of four Sab galaxies. See Section 6.3 for details. See Figure 8 for information on the overplotted lines and the Hubble type.

6.3 Implications for Interpreting the Hubble Sequence

Trends in integrated star formation activity along the Hubble sequence have been very well studied. Most observational studies have shown that global star formation varies significantly along the Hubble sequence, with star formation per unit stellar mass increasing from E-S0 through to Sd galaxies (see Kennicutt 1998a, for a review). However, these trends appeared to be much weaker when examining the nuclei of spiral galaxies. The results on the 24 μm morphologies here provides additional insights into why the variations are seen primarily in the galaxies' discs and how the galaxies' morphologies are tied to star formation in the discs.

A number of mechanisms have been proposed for building galaxies with larger bulges or galaxies that appear to have larger bulges. First, inequal mass merger events may transform smaller galaxies with modest bulge/disc ratios into larger galaxies with much larger bulge/disc ratios (e.g. Schweizer 1998, Sections 5.5 and 5.6). Second, pseudobulges can be formed when bars or other dynamical mechanisms funnel gas into the centres of galaxies (Kormendy & Kennicutt 2004). While not true bulges, these pseudobulges may look like bulges when viewed face-on and may result in galaxies being classified as early-type spiral galaxies. Third, in cluster environments, ram pressure stripping may remove gas from the discs of spiral galaxies (Gunn & Gott 1972). As the stellar populations evolve, the

discs, where star formation is repressed, become fainter compared to the nuclei, where gas is still present and where star formation continues. Such galaxies would appear to have large bulge/disc ratios and would be classified as early-type spiral galaxies or S0 galaxies.

In each of the above scenarios, the changes in the distribution of the ISM in the galaxies should be very similar. In the merger scenario, the gas will fall into the centre of the galaxy. In the pseudobulge scenario, the dynamical effects that create the pseudobulge also move the ISM into the centres of the galaxies. In the ram pressure stripping scenario, the only remaining ISM in the galaxies is located in the centres of the galaxies. Overall, all of these mechanisms will make the ISM appear more centralized in early-type spiral and S0 galaxies when compared to late-type spiral galaxies.

This is exactly what is seen in the 24 μm data presented here. Disc galaxies with large bulges (S0-Sab galaxies) generally have more centrally concentrated dust emission than disc galaxies with smaller bulges (Sc-Sd galaxies). Figure 8 and the analysis in Section 4 clearly illustrate this trend. As an additional demonstration of the effects of these evolutionary processes, Figure 12 shows four examples of Sab galaxies that have undergone different evolutionary processes. NGC 4826, a galaxy that contains counterrotating gas in its disc (Braun et al. 1992), is a good example of an inequal-mass merger remnant. Note the compact, asymmetric structure in the 24 μm image. NGC 4736 is a good example of a galaxy with a pseudobulge (Kormendy & Kennicutt 2004). Although faint spiral arms are present in the outer disc, the nucleus and inner ring are the two most prominent sources of 24 μm emission within this galaxy, making it appear very compact. NGC 4569, which lies within the Virgo Cluster, is an example of a galaxy that has undergone ram pressure stripping (Koopmann & Kenney 2004). Almost no emission originates from the disc of this galaxy. Although these three galaxies have evolved differently, the end result has been the same: a relatively large optical bulge/disc ratio, and relatively compact 24 μm emission.

In contrast to all of these, NGC 3031 is shown as an example of a Sab field galaxy with a "classical" bulge (Kormendy & Kennicutt 2004) that has not evidently undergone a recent merger (although it is interacting with other nearby galaxies). This galaxy is relatively extended compared to most other S0/a-Sab galaxies, and it qualitatively and quantitatively appears similar to many late-type spiral galaxies at 24 μm. Along with NGC 4725, it may be representative of a subset of early-type spiral galaxies that do not follow the same trends in 24 μm morphology as most other early-type spiral galaxies. Hence, the processes that are responsible for creating the real or apparent large bulge-to-disc ratios in many of the early-type spiral galaxies in this sample may not be responsible for the formation of the large bulges in early-type spiral galaxies like NGC 3031 and NGC 4725.

While acknowledging some exceptions, we may conclude that the distribution of 24 μm emission within spiral galaxies is a fundamental property linked to galaxies' Hubble classification. The results from the 24 μm data might also be indicative of the variations in the distribution of the cool dust or the cool ISM (neutral atomic and molecular hydrogen gas). However, the 24 μm emission is affected by dust heating as well as dust mass, so it is imperfect as a tracer of gas or dust mass; additional research is needed to determine the relation between morphological type and variations in the distribution of other components of the ISM.

Nonetheless, if the spatial distribution of the 24 μm emission is similar to that for cool gas and dust, then the variations observed here demonstrate that the secular processes that increase the real or apparent bulge/disc ratios of disc galaxies also change the distribution of the ISM within the galaxies. The ISM in the resulting S0 and early-type spiral galaxies is very centrally concentrated. Denied the fuel needed for star formation, the stellar populations in the discs of early-type spiral galaxies will appear older than in late-type spiral galaxies, contributing to the differences in relative star formation activity summarized by Kennicutt (1998a). The nuclei of these early-type spiral galaxies, however, will still have the fuel needed for star formation activity, which is why the nuclei of early- and late-type galaxies are difficult to distinguish in terms of star formation activity as discussed by Kennicutt (1998a).

6.4 The Variation in the Distribution of Infrared Emission in Dwarf Galaxies

Wide variations in the distribution of either star formation or the ISM in dwarf galaxies have been observed previously. For example, Parodi & Binggeli (2003), using optical data, found that star formation complexes were non-uniformly distributed throughout individual dwarf irregular galaxies. Hunter & Elmegreen (2006) found that some galaxies have centres that are bluer and more peaked than the centres of other dwarfs, demonstrating that star formation in dwarfs is sometimes centralized and sometimes diffuse. Begum et al. (2006) have found that H I was also distributed in an irregular and clumpy distribution.

The large range in the 24 μm morphologies of dwarf galaxies found in this paper generally reflects these previous results from the literature. The general amorphous morphology of the dwarf galaxies reflects the stochastic nature of star formation within these galaxies, as has been noted for some of the individual objects in this sample (e.g. Cannon et al. 2005). Under these circumstances, dust emission may no longer be expected to trace star formation well, as extinction may be variable across the galaxies (Cannon et al. 2005, e.g.) and large reservoirs of gas and dust not associated with star formation may be present in some galaxies (e.g. Begum et al. 2006; Walter et al. 2007).

7 CONCLUSIONS

The main results are as follows:

1. Statistically significant variations are seen in the 24 μm morphologies of nearby galaxies, and significant differences are seen between S0/a-Sab and Sc-Sd galaxies. Early-type galaxies generally have symmetrical, centrally concentrated 24 μm emission. Late-type galaxies generally have asymmetric, extended 24 μm emission. The variations along the Hubble sequence can be attributed to a number of mechanisms that transform late-type galaxies into early-type galaxies, including mergers, pseudobulge formation, and ram-pressure stripping in clusters.

2. The 24 μm morphologies of Sdm-Im galaxies are quite

varied. Some appear to be compact, point-like sources. Others appear to be highly extended and disorganized. Additionally, we noted that some dwarf galaxies were non-detections in one or more MIPS bands, implying weak or negligible star formation activity. This basically mirrors other results on the distribution of star formation or the ISM in nearby galaxies. The variability in the 24 μm morphologies reflects the stochastic nature of star formation within these galaxies.

3. Bars may make the 24 μm morphologies appear more centrally concentrated, thus confirming that bars play a role in enhancing nuclear star formation activity. However, the statistical significance of the results based on this sample are weak.

4. The trends in the 24 μm morphologies along the Hubble sequence mirror trends in morphological parameters measured in wave bands dominated by stellar emission. However, the 24 μm morphological parameters appear similar to the R-band morphological parameters for mergers and starbursts. These results indicate that morphological parameters measured in a wave band sensitive to star formation may not correspond to parameters measured in a wave band that traces older stellar populations.

5. The trends in the 24 μm morphologies along the Hubble sequence, including the differences between S0/a-Sab and Sc-Sd galaxies, appear similar to previously-observed trends in dust and molecular gas emission. However, the trends appear contrary to HI observations of nearby galaxies, which show no variations in the distribution of HI between early- and late-type spiral galaxies. Further observations are needed to understand the variations in the distribution of the multiple constituents of the ISM and their interrelation.

The implications of these results are extensive. Any proposed galaxy formation mechanisms that distinguish between early- and late-type galaxies or any proposed mechanisms that transform late-type galaxies into early-type galaxies must account for the variations in the distribution of the star formation. Moreover, models of the star formation histories of nearby galaxies must account for the differences in the location of star formation activity between early- and late-type spiral galaxies. In other words, valid models of spiral galaxies with large bulges cannot be created simply by adding large bulges with old stellar populations to star-forming discs but must account for how the location of star formation varies with the bulge-to-disc ratio.

We also note that the results here demonstrate that research based on infrared observations of one galaxy should be used cautiously. Such studies are able to examine multiwavelength dust emission in more detail and can provide detailed analyses on the nature of the emission. However, the applicability of the results on dust emission for single galaxies to galaxies of different Hubble types may be limited. At least in terms of the distribution of 24 μm emission, some galaxies are not even representative of galaxies with similar Hubble types. The distribution of 24 μm emission in NGC 3031, for example, cannot be treated as representative of all Sab galaxies, and NGC 6946 is not representative of all Scd galaxies. If other galaxy properties are linked to the spatial extent of the dust emission or at least the 24 μm emission (as suggested by Dale et al. 2007, , for example), then studies of individual objects like NGC 3031 and NGC 6946 might not be applicable to galaxies with similar Hubble types.

While the sample used in this work was adequate for uncovering morphological differences among nearby galaxies, a much larger sample would provide more statistically robust results and may also provide additional insights as to the circumstances where exceptions from morphological trends occur. An unbiased sample, such as a distance-limited sample, may also produce more robust results than the sample used here, as explained in Section 2.1. Additionally, larger samples of both field and cluster galaxies may demonstrate the extent to which interactions within clusters, particularly ram-pressure stripping, alter the distribution of dust emission or star formation within galaxies.

ACKNOWLEDGEMENTS

We would like to acknowledge D. Hollenbach and the reviewer for their helpful comments. Support for this work, part of the Spitzer Space Telescope Legacy Science Program, was provided by NASA through contract 1224769 issued by the Jet Propulsion Laboratory, California Institute of Technology under NASA contract 1407.

APPENDIX A: FINDING THE CENTRE POSITIONS FOR MEASURING THE $\overline{M}_{20}$ AND A PARAMETERS

To find the central position for calculating $\overline{M}_{20}$ and A, we adapted some of the procedures used by Lotz et al. (2004). To measure the $\overline{M}_{20}$, they recommend shifting the centre position for measuring radius until M_{tot} is minimised. To measure A, they recommend shifting the centre of rotation for the rotated image.

We measured $\overline{M}_{20}$ and A after shifting the centre positions to a series of locations within a 13×13 grid, with the centre of the grid corresponding to the central position given in RC3 and the grid positions spaced by 0.5 pixels (0.75 arcsec) to a maximum distance of 3 pixels (4.5 arcsec) from the RC3 position. We determined that when M_{tot} or A were minimised for centre positions further than 1 pixel (1.5 arcsec) from the RC3 position and when the corrections to $\overline{M}_{20}$ and A were $\gtrsim$5%, the objects were inherently asymmetric. In these situations, the positions corresponding to these minima probably are not the centres of the objects but are instead positions where asymmetric structures may have less of an effect on the measured $\overline{M}_{20}$ and A. Objects where M_{tot} was minimised for centre locations within 1 pixel of the RC3 position and where the change in $\overline{M}_{20}$ or A were $\gtrsim$5 were compact, off-center sources. The positions corresponding to these minima are certainly the centres of these objects.

We therefore determined that shifting the centre position away from the position given by RC3 was only appropriate if a minimum was found within 1 pixel. Thus, when M_{tot} or A were minimised when the centre position was shifted up to 1 pixel of the RC3 position, we used that position for measuring $\overline{M}_{20}$ or A. However, when M_{tot} or A were minimised when the centre position was shifted further than 1

pixel from the RC3 position, we used the RC3 position itself as the centre position.

REFERENCES

Abraham, R. G., Tanvir, N. R., Santiago, B. X., Ellis, R. S., Glazebrook, K., & van den Bergh, S., 1996, MNRAS, 279, L47

Athanassoula, E., 1992, MNRAS, 259, 345

Begum, A., Chengalur, J. N., Karachentsev, I. D., Kaisin, S. S., & Sharina, M. E., 2006, MNRAS, 365, 1220

Bendo, G. J., et al., 2002, AJ, 123, 3067

Bendo, G. J.,& Joseph, R. D., 2004, AJ, 127, 3338

Bendo, G. J., et al., 2006a, ApJ, 645, 134

Bendo, G. J., et al., 2006b, ApJ, 652, 283

Bershady, M. A., Jangren, A., & Conselice, C. J., 2000, AJ, 119, 2645

Bournaud, F., Combes, F., Jog, C. J, & Puerari, I., 2005, A&A, 438, 507

Braun, R., Walterbos, R. A. M., & Kennicutt, R. C., Jr., 1992, Nat, 360, 442

Buta, R., 1988, ApJS, 66, 233

Calzetti, D., et al., 2005, ApJ, 633, 871

Cannon, J. M., et al., 2005, ApJ, 630, L37

Cannon, J. M., et al., 2006, ApJ, 647, 293

Conselice, C. J., 2003, ApJS, 147, 1

Conselice, C. J., Bershady, M. A., & Jangren, A. 2000, ApJ, 529, 886

Dale, D. A., Giovanelli, R., Haynes, M. P., Hardy, E., Campusano, L. E. ,2001a, AJ, 121, 1886

Dale, D. A., Helou, G., Contursi, A., Silbermann, N. A., & Kolhatkar, S., 2001b, ApJ, 549, 215

Dale, D. A., et al., 2005, ApJ, 633, 857

Dale, D. A., et al., 2007, ApJ, 655, 863

de Vaucouleurs, G., de Vaucouleurs, A., Corwin, H. G., Buta, R. J., Paturel, G., & Fouque, P., 1991, Third Reference Catalogue of Bright Galaxies, Springer-Verlag, Berlin

Devereux, N. A., & Young, J. S., 1993, AJ, 106, 948

Fazio, G. G., et al., 2004, ApJS, 154, 10

Friedli, D., & Benz, W., 1993, A&A, 268, 65

Gordon, K. D., et al., 2004, ApJS, 154, 215

Gordon, K. D., et al., 2005, PASP, 117, 50

Gunn, J. E., & Gott, J. R., III, 1972, ApJ, 176, 1

Ho, L. C., Filippenko, A. V., & Sargent, W. L. W., 1997a, ApJ, 487, 591

Ho, L. C., Filippenko, A. V., & Sargent, W. L. W., 1997b, ApJS, 112, 315

Hodge, P. W., & Kennicutt, R. C., Jr., 1983, ApJ, 267, 563

Huang, J. H., Gu, Q. S., Su, H. J., Hawarden, T. G., Liao, X. H., & Wu, G. X., 1996, A&A, 313, 13

Hubble, E., 1926, ApJ, 64, 321

Hunter, D. A., & Elmegreenn, B. G., 2006, ApJS, 162, 49

Kennicutt, R. C., Jr., 1998a, ARA&A, 36, 189

Kennicutt, R. C., Jr., 1998b, ApJ, 498, 541

Kennicutt, R. C., Jr., et al., 2003, PASP, 115, 928

Koopmann, R. A., Haynes, M. P., & Catinella, B., 2006, AJ, 131, 716

Koopmann, R. A., & Kenney, J. D. P., 2004, ApJ, 613, 866

Kormendy, J., & Kennicutt, R. C., Jr., 2004, ARA&A, 42, 603

Krist, J., 2002, Tiny Tim/SIRTF User's Guide, SSC, Pasadena

Li, A., & Draine, B. T., 2001, ApJ, 554, 778

Lotz, J. M., Primack, J., & Madau, P., 2004, AJ, 128, 163

Lu, N., et al., 2003, ApJ, 588, 199

Martinet, L., & Friedi, D., 1997, A&A, 323, 363

Pahre, M. A., Ashby, M. L. N., Fazio, G. G., & Willner, S. P., 2004, ApJS, 154, 235

Parodi, B. R., & Binggeli, B., 2003, A&A, 398, 501

Perez-Gonzalez, P. G., et al., 2006, ApJ, 648, 987

Puxley, P. J., Hawarden, T. G., & Mountain, C. M., 1988, MNRAS, 234, 29P

Rand, R. J., Kulkarni, S. R., Hester, J. J., 1992, ApJ, 396, 97

Regan M. W., et al., 2006, ApJ, 652, 1112

Rieke, G. H., et al., 2004, ApJS, 154, 25

Roberts, M. S., & Haynes, M. P., 1994, ARA&A, 32, 115

Roussel, H., et al., 2001, A&A, 372, 406

Sakamoto, K., Okumura, S. K., Ishizuki, S., & Scoville, N. Z., 1999, ApJ, 525, 691

Schweizer, F., 1980, ApJ, 237, 303

Schweizer, F., 1998, in Friedli D., Martinet L., & Pfenniger D., eds, Galaxies: Interactions and Induced Star Formation, Springer-Verlag, Berlin, p. 105

Sheth, K., Vogel, S. N., Regan, M. W., Thornley, M. D., & Teuben, P. J., 2005, ApJ, 632, 217

SINGS Team, 2006, User's Guide, SSC, Pasadena

Spitzer Science Center, 2006, *Spitzer* Observer's Manual Version 7.1, SSC, Pasadena

Taylor, C. L., Kobulnicky, H. A., & Skillman, E. D. 1998, ApJ, 116, 2746

Thomas, H. C., Alexander, P., Clemens, M. S., Green, D. A., Dunne, L., & Eales, S., 2004, MNRAS, 351, 362

Telesco, C. M., Dressel, L. L., & Wolstencroft, R. D., 1993, ApJ, 414, 120

Tully, R. B., 1988, Nearby Galaxies Catalog, Cambridge University Press, Cambridge

Turner, J. L., & Ho, P. T. P., 1983, ApJ, 268, L79

Wade, C. M., 1961, Pub. NRAO, 1, 99

Walter, F., et al., 2007, preprint (astro-ph/0702378)

Young, J. S. & Knezek, P. M., 1989, ApJ, 347, L55

Young, J. S., et al., 1995, ApJS, 98, 219